A Keck/DEIMOS spectroscopic survey of the faint M31 satellites And IX, And XI, And XII and And XIII[★][†]

M. L. M. Collins,[1][‡] S. C. Chapman,[1] M. J. Irwin,[1] N. F. Martin,[2] R. A. Ibata,[3]
D. B. Zucker,[4,5] A. Blain,[6] A. M. N. Ferguson,[7] G. F. Lewis,[8] A. W. McConnachie[9]
and J. Peñarrubia[1]

[1]*Institute of Astronomy, Madingley Road, Cambridge CB3 0HA*
[2]*Max-Planck-Institut for Astronomy, Königstuhl 17, D-69117 Heidelberg, Germany*
[3]*Observatoire de Strasbourg, 11 rue de l'Université, F-67000 Strasbourg, France*
[4]*Macquarie University, NSW 2109, Australia*
[5]*Anglo-Australian Telescope, PO Box 296, Epping, NSW 1710, Australia*
[6]*California Institute of Technology, 1200 E. California Blvd, MC 105-24 Pasadena, CA 91125, USA*
[7]*Institute for Astronomy, University of Edinburgh, Royal Observatory, Blackford Hill, Edinburgh EH9 3HJ*
[8]*Sydney Institute for Astronomy, School of Physics, A29 University of Sydney, NSW 2006, Australia*
[9]*NRC Herzberg Institute of Astrophysics, 5071 West Saanich Road, Victoria V9E 2E7, Canada*

ABSTRACT

We present the first spectroscopic analysis of the faint M31 satellite galaxies, And XI and And XIII, as well as a re-analysis of existing spectroscopic data for two further faint companions, And IX (correcting for an error in earlier geometric modelling that caused a misclassification of member stars in previous work) and And XII. By combining data obtained using the Deep Imaging Multi-Object Spectrograph (DEIMOS) mounted on the Keck II telescope with deep photometry from the Suprime-Cam instrument on Subaru, we have identified the most probable members for each of the satellites based on their radial velocities (precise to several $\mathrm{km\,s^{-1}}$ down to $i \sim 22$), distance from the centre of the dwarf spheroidal galaxies (dSphs) and their photometric [Fe/H]. Using both the photometric and spectroscopic data, we have also calculated global properties for the dwarfs, such as systemic velocities, metallicities and half-light radii. We find each dwarf to be very metal poor ([Fe/H] ~ -2 both photometrically and spectroscopically, from their stacked spectrum), and as such, they continue to follow the luminosity–metallicity relationship established with brighter dwarfs. We are unable to resolve dispersion for And XI due to small sample size and low signal-to-noise ratio, but we set a 1σ upper limit of $\sigma_v < 4.5\,\mathrm{km\,s^{-1}}$. For And IX, And XII and And XIII we resolve velocity dispersions of $\sigma_v = 4.5^{+3.6}_{-3.4}$, $2.6^{+5.1}_{-2.6}$ and $9.7^{+8.9}_{-4.5}\,\mathrm{km\,s^{-1}}$, though we note that the dispersion for And XIII is based on just three stars. We derive masses within the half-light radii for these galaxies of $6.2^{+5.3}_{-5.1} \times 10^6$, $2.4^{+6.5}_{-2.4} \times 10^6$ and $1.1^{+1.4}_{-0.7} \times 10^7\,\mathrm{M_\odot}$, respectively. We discuss each satellite in the context of the Mateo relations for dSphs, and in reference to the universal halo profiles established for Milky Way dwarfs. Both And IX and And XII fall below the universal halo profiles of Walker et al., indicating that they are less massive than would be expected for objects of their half-light radius. When combined with the findings of McConnachie & Irwin, which reveal that the M31 satellites are twice as extended (in terms of both half-light and tidal radii) as their Milky Way counterparts, these results suggest that the satellite population

of the Andromeda system could inhabit haloes that with regard to their central densities are significantly different from those of the Milky Way.

Key words: galaxies: abundances – galaxies: dwarf – galaxies: kinematics and dynamics – Local Group – dark matter.

1 INTRODUCTION

In recent years, the low-luminosity population of dwarf spheroidal galaxies (dSphs) has drastically increased in number, with ∼30 faint satellites discovered both within the halo of our Milky Way (MW) and in that of our 'sister' galaxy, M31 (e.g. Zucker et al. 2004, 2006a,b, 2007; Willman et al. 2005b; Martin et al. 2006, 2009; Belokurov et al. 2008; Irwin et al. 2008; McConnachie et al. 2008). Whilst in principle these minuscule stellar associations should be some of the simplest objects of the galactic family – which spans roughly seven orders of magnitude in mass – to understand, the analysis of faint dSphs ($M_V > -8$) within the MW has dissolved the notion that they form in a simple, homogeneous fashion. Detailed studies (both photometric and spectroscopic) of such objects reveal several unusual properties for the population. For example, they highlight a significant departure from the well-established mass–luminosity relationship for dSphs (Mateo 1998). A number of these newly discovered objects are also quite controversial in their nature, possessing properties that are common to both dSphs and globular clusters and are therefore difficult to classify as either, such as the unusual objects, Willman 1 and Segue 1 (Willman et al. 2005a; Belokurov et al. 2007; Niederste-Ostholt et al. 2009). In addition, comparisons of the MW and M31 dSph systems have revealed significant differences between the populations, where the classical M31 dwarfs ($M_V < -8$) are observed to be at least twice as extended as their MW counterparts, in terms of both their half-light and tidal radii (McConnachie & Irwin 2006b). In addition, the spatial distribution of the M31 satellites around their host is more extended than the Galactic satellite distribution, with approximately half of the Galactic satellites found within 100 kpc of the Galaxy, compared to roughly 200 kpc for M31 (Koch & Grebel 2006; McConnachie & Irwin 2006a). Such differences indicate that environment plays a significant role in the evolution of dSphs, the full extent of which is not known.

Another significant point of interest concerning dwarf galaxies is the well known discrepancy between the observed number of these satellites, and the number predicted by Λ cold dark matter (ΛCDM) models in numerical simulations (e.g. Klypin et al. 1999; Moore et al. 1999), which still amounts to one to two orders of magnitude. Survey completeness is likely to contribute to at least part of this deficit (see e.g. Willman et al. 2004; Simon & Geha 2007; Koposov et al. 2008; Tollerud et al. 2008; McConnachie et al. 2009); as in the Galactic case, observational efforts are hampered by obscuration from the disc and the bulge. It is thought that future all-sky surveys may find a wealth of ultrafaint satellites that would reduce the gap between observation and theory. Other explanations assume that many of these haloes would remain dark to the present day, owing to suppression of star formation as the result of a photoionizing background (Somerville 2002). These haloes would therefore represent a significant proportion of the satellite haloes found in simulations, reconciling these with observations.

In an attempt to better understand this unusual population of galaxies, and to unite theory with observation, spectroscopic sur-veys of faint dwarf galaxies [particularly within the MW via the Sloan Digital Sky Survey (SDSS)] have been carried out. Using the velocity information from the spectra, one can measure the systemic velocities and intrinsic velocity dispersions for these objects, which can be used to estimate the mass of these systems (e.g. Illingworth 1976; Richstone & Tremaine 1986; Walker et al. 2009b; Wolf et al. 2010). However, methods such as these make various assumptions about the anisotropy and virial equilibrium of the systems that are not necessarily correct. None the less, such methods have been shown to be good indicators of the instantaneous mass of the system (e.g. Oh, Lin & Aarseth 1995; Piatek & Pryor 1995; Muñoz, Majewski & Johnston 2008), and can therefore provide an insight into the mass distribution of the satellites. Historically, the results of such studies indicated the existence of a mass limit of ∼10^7 M$_\odot$ under which no dwarf galaxies are found, supporting the theory that these satellites would indeed only inhabit massive dark matter haloes. The existence of such a mass limit would confirm the empirical relation defined by Mateo (1998) for satellites that are brighter than Draco ($M_V = -8.8$) and Ursa Minor ($M_V = -8.9$) in the Local Group: $M/L = 2.5 + (L/10^7 \, L_\odot)$, where M/L is the mass-to-light ratio of the galaxies and L is their luminosity. Work by Strigari et al. (2008), investigating the mass contained within the central 300 pc of dSphs, reinforced this relation, demonstrating that, despite the studied dSphs spanning five orders of magnitude in luminosity, they appear to show a lower dynamical mass limit of ∼10^7 M$_\odot$. However, such a finding is in stark contrast with the masses derived for some of the recently discovered ultrafaint dSphs, e.g. Segue 1 and Leo V, whose masses of ∼10^5 M$_\odot$ (Geha et al. 2009; Walker et al. 2009a) fall well below this bound. This discrepancy has been addressed in work by Walker et al. (2009b), where they evaluate the mass of dSphs within the half-light radius ($r_{1/2}$). Their analysis shows that these ultrafaint dSphs may simply be more deeply embedded within dark matter haloes that are similar to those inhabited by their larger and brighter counterparts (also discussed in Peñarrubia, McConnachie & Navarro 2008a), which could suggest the existence of a 'universal' dark matter halo. Similar results are shown in Wolf et al. (2010), where they conclude that all the MW dSphs are consistent with inhabiting dark matter haloes with a mass $M_{\rm halo} \sim 3 \times 10^9$ M$_\odot$. The recently discovered faint dSphs described above populate the faint end of the satellite luminosity function, and their spectroscopic analysis would allow us to see if these objects are indeed highly dark matter dominated, and whether they conform to such a mass limit.

Until recently, only a handful of the M31 dSphs have been analysed spectroscopically [And II, And IX, And XII, And XIV, And XV, And XVI and And X (Côté et al. 1999; Chapman et al. 2006, 2007; Majewski et al. 2007; Kalirai et al. 2009; Letarte et al. 2009)], with only one of these (And XII by Chapman et al. 2007) probing the fainter end of the luminosity function ($M_V > -8$). A recent paper by Kalirai et al. (2010) has extended the number of bright dSphs surveyed, presenting new data for And I, And II and And III, but the kinematic properties of M31's lowest luminosity dSphs are still unknown. Spectroscopic observations of these

objects would allow us to see how they compare to both their brighter M31 brethren, and their MW cousins of a comparable luminosity.

As a step towards this end, we have initiated a kinematic survey of the trio of faint dwarfs discovered by Martin et al. (2006), And XI, And XII and And XIII using the Deep Imaging Multi-Object Spectrograph (DEIMOS) on Keck II. We combine these kinematics with deep photometry from Suprime-Cam on the Subaru telescope. The analysis of our observations is performed here for these objects, including a re-treatment of And XII, whose orbital properties were modelled in Chapman et al. (2007), but whose detailed properties were not assessed. We also include a re-examination of the faint satellite, And IX, using the same spectroscopic data as Chapman et al. (2005), as there was an error in the geometric modelling of the slit mask used to calculate the velocities, which led to a misclassification of member stars; this has since been corrected for, and we also present additional Subaru photometry for the satellite. The outline of the paper is as follows: Section 2 presents the observing strategy, the observations and how they were reduced ; Section 3 is dedicated to the analysis of And XI, And XII And XIII and And IX; we discuss our findings in Section 4 and provide conclusions in Section 5.

2 OBSERVATIONS

2.1 Photometric observations

Each of the satellites were observed photometrically using the Suprime-Cam instrument, mounted on the primary focus of the 8-m Subaru telescope, located at the summit of Mauna Kea. This instrument is ideal for probing the spatial extent of these faint dwarfs as it can reach the horizontal branch (HB) of populations at distances greater than 500 kpc in a reasonable exposure time. Furthermore, it has a wide field of view (34×27 arcmin^2) which is more than sufficient to cover the entire region of the dwarfs at the distance of M31.

Observations of And XI, And XII and And XIII were made on the night of 2006 September 22, in photometric conditions with an average seeing of 0.6 and 0.5 arcsec in the *g* and *i* bands, respectively. For these satellites we exposed for a total of 2100 s in *g* band (split into 5×420 s dithered subexposures) and 4800 s in the *i* band (split into 20×240 s subexposures) in an attempt to reach below the HB to an equal depth in both bands. The data were processed using the CASU general purpose pipeline for processing wide-field optical CCD data (Irwin & Lewis 2001). The images were debiased and trimmed before being flat-fielded and gain-corrected to a common internal system using master flats constructed from twilight sky observations. Catalogues were generated for every science image and used to refine the astrometric alignment of the images. The images were then grouped for individual objects and passbands and stacked to form the final science images based on the updated astrometry. A catalogue was then generated for each final stacked science image, objects morphologically classified as stellar, non-stellar or noise like, and the *g, i* band catalogue data merged. As a final step, for And XI, And XII and And XIII the *g, i* Subaru data was calibrated with respect to our MegaCam system *g, i* using all stellar objects in common with signal-to-noise ratio (S/N) >10. And IX was observed in service mode during the period 2004 October 9–10 with typically subarcsecond seeing, for a total of 600 s in each of *g, r* and *i* bands (split into 5×120 s dithered subexposures for each filter). The data were reduced in a similar manner to those for And XI, And XII and And XIII, although here, the photometry from

the CASU Subaru pipeline was matched to the SDSS M31 scan data.

The data for all satellites are extinction corrected and dereddened using the Schlegel, Finkbeiner & Davis (1998) dust maps. We find $E(B - V) = 0.08$ for And XI, And XIII and And IX, and $E(B - V) = 0.12$ for And XII.

2.2 Spectroscopic observation

For each of the dSphs in question, candidate members were selected using colour–magnitude diagrams (CMDs) from the Canada–France–Hawaii Telescope (CFHT) as shown in Fig. 1 where we present the MegaCam colours (without correcting for extinction and reddening) for the stars within these objects, transformed into Landolt V and I using a two-stage process detailed in Ibata et al. (2007) and McConnachie et al. (2004). Colour–magnitude boxes were used to select red giant branch (RGB) stars that lay within 3–5 arcmin regions surrounding each of the satellites, which is equivalent to several half-light radii of these objects. DEIMOS is a multislit, double-beam spectrograph mounted on the Nasmyth focus of the Keck II telescope on Mauna Kea, ideal for taking optical spectra of faint objects such as these. For And XI, And XII and And XIII multi-object observations were taken from 2006 September 21–24 with DEIMOS in photometric conditions and with excellent 0.6-arcsec seeing. Our chosen instrumental setting covered the observed wavelength range from 5600 to 9800 Å with exposure time of 3×20 min integrations. The RGB stars in these three new dwarfs are faint ($i = 21.5$–23.0), so to obtain a useful S/N in a reasonable exposure time, all the spectra employ the low resolution (~ 3.5 Å) 600 line mm^{-1} grating. And IX was observed on the night of 2004 September 13 under photometric conditions with seeing from 0.5 to 0.8 arcsec. We employed the 1200 line mm^{-1} grating, covering the wavelength range 6400–9000 Å, also with exposure time of 3×20 min integrations. Data reduction was performed using the DEIMOS-DEEP2 pipeline (Faber et al. 2003), which included debiasing, flat-fielding, extracting, wavelength calibrating and sky subtracting the spectra. In Table 1, we detail the positions targeted by each mask, the number of target stars and the total number of stars for which accurate velocities were derived (discussed further below).

The kinematic data for And IX were originally presented in Chapman et al. (2005). However, the geometric model used for the slit mask was incorrect, causing a shift in the measured velocities of the observed stars of order 5 km s^{-1}, which has been corrected in this work. This systematic error caused a misclassification of member stars within the sample, which in turn affected the measurements of systemic velocity, dispersion and metallicity for the satellite in Chapman et al. (2005). The velocities for all observed stars have since been re-measured allowing us to correctly derive the properties of And IX in this work.

2.2.1 Velocity calculations and error analysis

Our instrumental set-up covered the wavelength range of the calcium II (Ca II) triplet, a strong absorption feature centred at ~ 8550 Å. To determine velocities for our targeted stars, we cross-correlated each spectrum with a model template of the feature at the rest-frame wavelength positions of the triplet lines (the technique used is similar to that discussed by Wilkinson et al. 2004). Briefly, we perform cross-correlations for each star with our template and compute the corrected heliocentric velocity for each star. We also compute the Tonry–Davis R value (TDR) for each cross-correlation, which is an
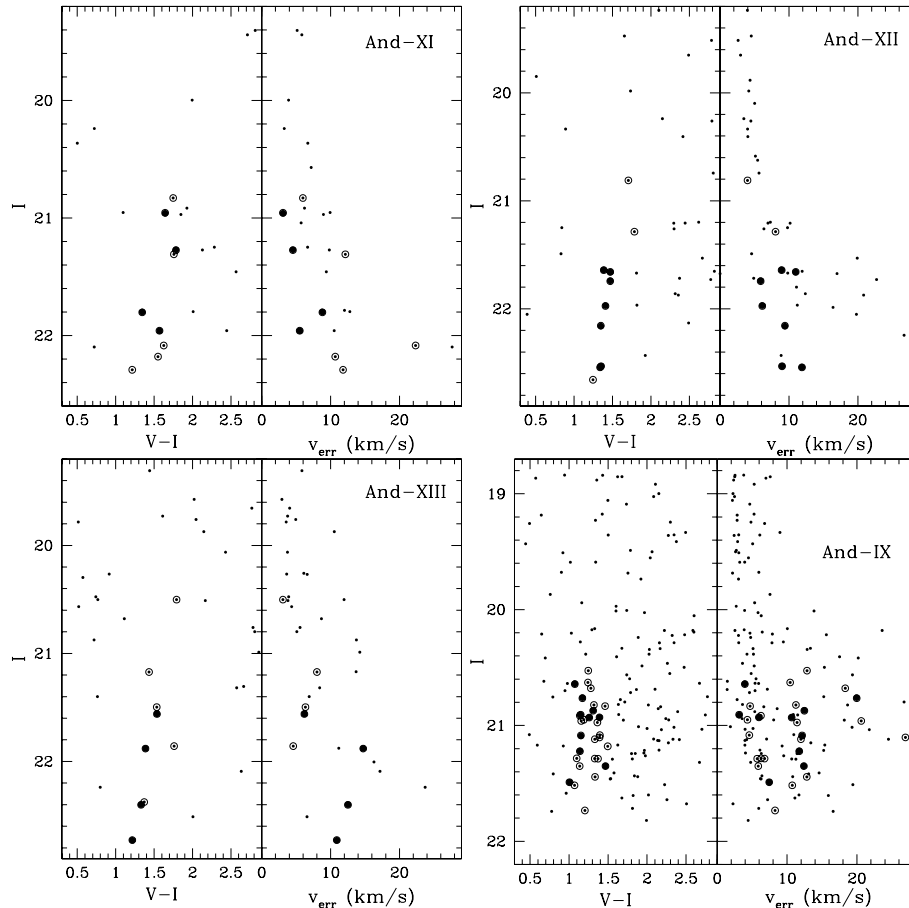
Figure 1. CFHT-MegaCam colour–magnitude diagrams (left-hand panel of each figure), where the native MegaCam *g* and *i* bands have been converted into *V* and *I* magnitudes using transformations detailed in McConnachie et al. (2004), Ibata et al. (2007) and radial velocity uncertainties (right-hand panel of each figure) of the observed stars in the four objects surveyed in the paper. The top left-hand panel corresponds to And XI, the top right to And XII and the bottom left and right correspond to And XIII and And IX, respectively. The small dots represent CFHT objects within approximately one half-light radius of each dSph, filled circles represent target stars selected in the satellites CMD RGB features. Circled points represent stars that were initially selected as field stars but have the radial velocity and the CMD position of dwarf stars and thus were used to derive the dwarf parameters.

Table 1. Details of the Keck/DEIMOS observations of And XI, And XII, And XIII and And IX.

Date observed (dd/mm/yyyy)	Mask α_{J2000}	Mask δ_{J2000}	Object	Grating	Field PA	Exp. time (s)	No. targets	No. reduced
23/09/2006	00:46:21	+33:48:21	And XI	600 line mm^{-1}	0°	3 × 1200	35	32
21/09/2006	00:47:27	+34:22:30	And XII	600 line mm^{-1}	0°	3 × 1200	50	48
23/09/2006	00:47:27	+34:22:30	And XII	600 line mm^{-1}	0°	3 × 1200	50	48
23/09/2006	00:51:51	+33:00:16	And XIII	600 line mm^{-1}	0°	3 × 1200	49	48
13/09/2004	00:52:51	+43:11:48	And IX	1200 line mm^{-1}	0°	3 × 1200	648	277

indication of the reliability of the resulting velocity. We consider any velocity cross-correlation with a TDR value ≥3.5 to be reliable. In Tables 2–5, we note the TDR values for each of our likely member stars (discussed in greater detail in Section 3). We also estimated the velocities for each star using a Doppler shift method, fitting Gaussians to each of the triplet lines individually and computing the mean velocity shift from these. The results of both calculations were generally found to be consistent (within ∼2–5 km s^{-1}) with one another. In a few instances, the Gaussian technique revealed cases where the cross-correlation technique had fixed on to a noise feature, rather than the true Ca II triplet, and these cases, we have taken the velocities derived from the Gaussian technique. However, as it is generally accepted that simple Doppler-shift velocities are

less reliable in low S/N data (e.g. Allende Prieto 2007), we refer to velocities computed by the cross-correlation method throughout the text, unless otherwise stated.

For the Ca II triplet lines, the spectral features of interest overlap in location with strong night sky OH recombination lines for some of the dSph members. While we are able to detect continuum at S/N ≥ 3 Å^{-1} for even the faintest (*i* = 23) stars observed, the velocity errors are subject to larger systematic errors when they lie close to these OH lines. This effect is seen most prominently in the case of And XII, where the Ca II$_{8498}$ line coincides with a strong sky feature. This effect is seen in the night-to-night variations in the velocities of the And XII stars, for which we obtained repeat observations. A systematic shift in the velocities between the two

Table 2. Properties of candidate member stars in And XI, centred at $\alpha = 00:46:21$, $\delta = +33:48:22$. Outlier at $v = -432.3$ km s^{-1} is also included as the last entry.

Star α	Star δ	Vel (km s^{-1})	[Fe/H]$_{spec}$	[Fe/H]$_{phot}$	S/N (Å^{-1})	TDR	I mag	V mag
00:46:22.65	+33:46:21.6	-418.8 ± 6.2	-2.42	-2.0	16.7	15.37	20.5	21.9
00:46:19.10	+33:48:4.1	-417.2 ± 6.3	-1.56	-1.5	13.5	17.2	20.8	22.3
00:46:15.14	+33:48:26.7	-419.8 ± 6.2	-0.61	-1.9	9.3	8.4	21.3	22.5
00:46:21.56	+33:48:22.4	-421.9 ± 6.4	-1.69	-1.4	7.8	7.3	21.5	22.9
0:46:16.96	+33:48:3.8	-432.3 ± 10.8	–	-1.8	6.0	3.4	21.8	22.9

Table 3. Properties of candidate member stars in And XII, centred at $\alpha = 00:47:27$, $\delta = +34:22:29$.

Star α	Star δ	Vel (km s^{-1})	[Fe/H]$_{spec}$	[Fe/H]$_{phot}$	S/N (Å^{-1})	TDR	I mag	V mag
00:47:31.04	+34:24:12.1	-566.9 ± 6.6	-2.4	-2.0	8.9	5.0	21.1	22.4
00:47:24.69	+34:22:23.9	-567.8 ± 6.3	-2.3	-1.7	10.1	10.7	21.2	22.5
00:47:27.76	+34:22:6.2	-549.8 ± 6.2	-1.7	-1.7	11.4	11.0	21.2	22.6
00:47:28.63	+34:22:43.1	-561.2 ± 6.3	-2.1	-1.8	9.7	8.9	21.5	22.8
00:47:31.34	+34:22:57.6	-549.3 ± 7.0	-1.9	-1.6	7.3	6.75	21.7	22.9
00:47:26.65	+34:23:22.8	-547.4 ± 6.5	-2.5	-1.7	6.2	5.97	22.0	23.3
00:47:27.18	+34:23:53.5	-557.8 ± 6.7	-2.0	-1.7	5.4	5.3	22.0	23.2
00:47:30.60	+34:24:20.3	-557.4 ± 7.3	-1.9	-1.5	4.8	3.7	22.2	23.3

Table 4. Properties of candidate member stars in And XIII, centred at $\alpha = 00:51:51$, $\delta = +33:00:16$.

Star α	Star δ	Vel (km s^{-1})	[Fe/H]$_{spec}$	[Fe/H]$_{phot}$	S/N (Å^{-1})	TDR	I mag	V mag
00:51:53.00	+33:00:18.2	-202.6 ± 6.2	-1.9	-1.7	9.9	16.2	21.0	22.4
00:51:49.81	+33:00:41.1	-195.7 ± 6.5	-1.9	-1.6	3.3	7.2	22.1	23.3
00:51:42.34	+32:58:05.3	-184.7 ± 6.6	-1.8	-1.9	4.7	5.9	21.9	23.1

Table 5. Properties of candidate member stars in And IX, centred at $\alpha = 00:52:51.1$, $\delta = +43:11:48.6$. The two stars with unreliable velocities (TDR < 3.5) and the contaminant star at $> r_t$ are also included as the last three entries.

Star α	Star δ	Vel (km s^{-1})	[Fe/H]$_{spec}$	[Fe/H]$_{phot}$	S/N (Å^{-1})	TDR	I mag	V mag
00:52:45.74	+43:12:53.6	-198.8 ± 5.8	-2.10	-2.77	2.6	4.5	20.8	21.9
00:52:53.18	+43:12:48.2	-208.3 ± 2.4	-2.20	-2.75	4.7	7.5	20.9	22.1
00:52:58.04	+43:11:40.6	-201.2 ± 5.1	-2.34	-2.04	2.7	4.1	20.9	22.2
00:52:58.96	+43:13:39.1	-215.0 ± 4.0	-1.90	-2.18	2.5	4.3	21.0	22.2
00:52:53.35	+43:12:41.3	-197.7 ± 6.0	-2.00	-2.55	3.1	8.3	21.1	22.2
00:52:52.30	+43:12:41.1	-210.7 ± 2.3	-1.75	-1.73	3.7	12.1	20.9	22.3
00:53:15.36	+43:14:11.1	-209.3 ± 12.1	-2.84	-2.98	3.2	2.7	21.5	22.5
00:52:50.32	+43:11:54.4	-201.7 ± 20.3	-2.90	-3.00	2.5	1.6	21.5	22.6
00:53:49.38	+43:12:20.0	-202.3 ± 4.5	-0.60	-0.61	3.1	5.0	21.6	23.9

nights of 30 km s^{-1} is observed for some of the stars, while other stars in the mask at more favourable velocities have night to night errors <5 km s^{-1}. For those stars where this effect is very prominent, we mask out the affected line and repeat the cross-correlation on the two unobscured lines.

There are a number of systematic errors that can be introduced into velocity calculations from the instrument set-up, such as the effect of slight mask rotation, field misalignment and improperly cut masks, all of which can cause the star to be miscentred within the slit, resulting in an incorrect velocity measurement that can range from a few to 10s of km s^{-1}. To correct for this error, we make use of telluric absorption features present within our spectra, particularly the strong Fraunhofer A-band telluric absorption feature located between 7600 and 7630 Å. These features are the result of absorption of stellar light by various gases (O$_2$, H$_2$O, CO$_2$, etc.) within the Earth's atmosphere. These lines are therefore not Doppler shifted, and should be present at the same wavelength in each spectrum. Following the techniques of Simon & Geha (2007) and Sohn et al. (2007), we construct a template telluric spectrum which can be cross-correlated with each of our science spectra to determine the effective velocity shift caused by these systematic errors. For the fields observed in this work, we found that the average velocity shift for each mask derived by this method ranged from +2.8 to +8.1 km s^{-1}. To correct our observed velocities for this, we add the velocity shift calculated for each star to our cross-correlation velocities determined from the Ca II triplet. In Fig. 2 we show the telluric corrections derived for And XII (average correction = 2.8 km s^{-1}) as a function of I-band magnitude and S/N. For brighter stars ($I < 21$) and stars with higher S/N (S/N > 15 Å^{-1}), the velocity corrections are approximately constant, however, for fainter stars (stars with lower S/N) the magnitude of this telluric correction shows significant scatter about the median value. It is therefore unclear whether this method can accurately compute the telluric shift in fainter objects.
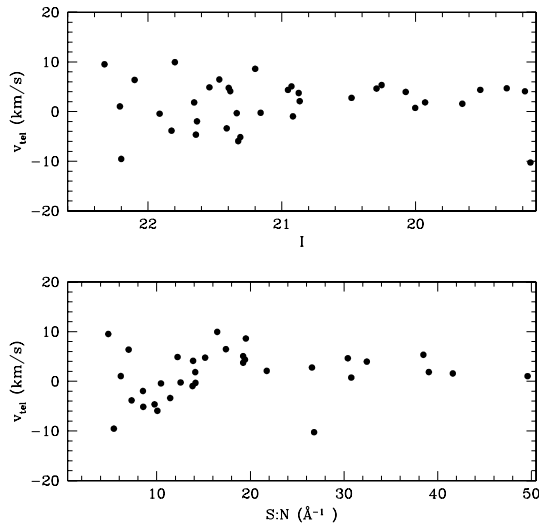
Figure 2. Telluric velocity corrections for all stars in And XII as a function of *I*-band magnitude (top) and S/N (bottom). The median telluric correction for this mask is 2.8 km s^{-1}, and for bright ($I < 21$), high S/N (S/N > 12 Å^{-1}) targets, this correction remains approximately constant. However for fainter stars with noisier spectra, this correction shows increased scatter about the median value.

We estimate the errors on our velocities by following the procedures of Simon & Geha (2007) and Kalirai et al. (2010). First, we make an estimate of our velocity uncertainties for each observed star using a Monte Carlo method, whereby noise is randomly added to each pixel in the spectrum, assuming a Poisson distribution for the noise. We then recalculate the velocity and telluric offset of each star, using the same cross-correlation method detailed above. This procedure is repeated 1000 times, and then the error is calculated to be the square root of the variance of the resulting mean velocity. Secondly, we make use of our And XII data set, where we were able to obtain repeat observations for our entire mask, giving us 47 stars with two velocity measurements, v_1 and v_2. We then attempt to measure our velocity errors directly by comparing these velocities and defining a normalized error, σ_N which incorporates our Monte Carlo error estimates for each measurement pair, σ_1 and σ_2, plus a random error, ϵ, which represents any uncertainties we have not accounted for. ϵ is defined as the additional random error required in order to reproduce a unit Gaussian distribution with our data (shown in Fig. 3). For the And XII stars, which were observed with the 600 line mm^{-1} grating, we find $\epsilon = 6.2$ km s^{-1}. While this is roughly double that found in other works (e.g. 2.2 km s^{-1} in Simon & Geha 2007 and ~3 km s^{-1} in Kalirai et al. 2010), we note that they use the 1200 line mm^{-1} grating, which has a resolution of ~1.3 Å compared to the 600 line mm^{-1} gratings resolution of ~3.5 Å. Therefore, for And XI, And XII and And XIII, we set $\epsilon = 6.2$ km s^{-1}, and we use Simon & Geha (2007) value of $\epsilon = 2.2$ km s^{-1} for And IX. We then combine this systematic error in quadrature with our calculated errors from the Monte Carlo technique (σ_{MC}), giving us our final error estimate. We display the errors for all observed stars in the four dSphs as a function of S/N in Fig. 4. The dSphs observed using the 600 line mm^{-1} grating (And XI, And XII and And XIII) are shown in the top panel, and And IX (observed with the 1200 line mm^{-1} grating) is shown in the lower panel. It can be seen in both cases that we can measure velocities to accuracies of ~5–15 km s^{-1} down to a S/N of 3 or better, while the higher S/N stars have velocity errors
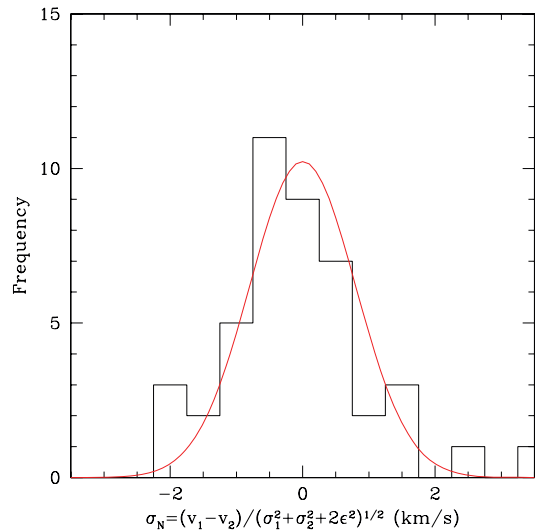

Figure 3. A histogram showing the normalized error distribution for repeat measurements of the same stars in our And XII data set. The normalized error, σ_N, incorporates the velocity differences between the repeat measurements (v_1 and v_2), and the Monte Carlo uncertainties calculated for each observation (σ_1 and σ_2). In order to reproduce a unit Gaussian distribution for our uncertainties, we also include an additional error term, ϵ, which accounts for any systematic uncertainties we have not included. For the And XII data (observed with the 600l grating), we find $\epsilon = 6.2$ km s^{-1}. For And IX, which was observed with the 1200l grating, we set $\epsilon = 2.2$ km s^{-1}, which was the value derived by Simon & Geha (2007) from repeat observations of stars in their Keck/DEIMOS survey, which used a similar observational set-up to that of And IX.
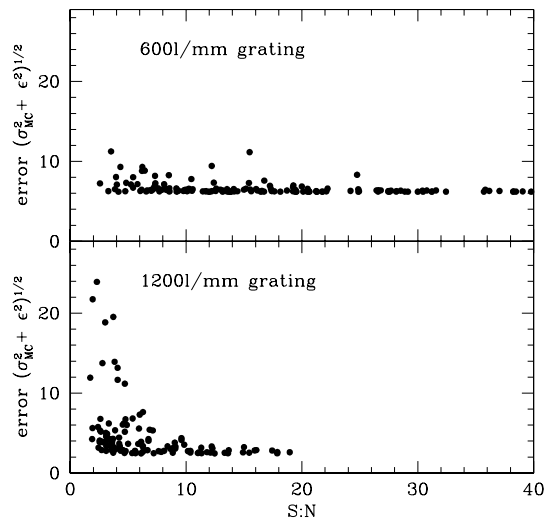

Figure 4. The total error in velocity of all stars observed within And XI, And XII and And XIII (top panel) and And IX (lower panel) as a function of S/N. The total error is calculated by combining the Monte Carlo error (σ_{MC}) discussed in Section 2.2.1, and the systematic error, ϵ (6.2 km s^{-1} for And XI, And XII and And XIII, 2.2 km s^{-1} for And IX), in quadrature. It can be seen that we can measure the velocities of our sample to accuracies of typically less than 15 km s^{-1} down to S/N $\geq$ 3 Å^{-1}.

that are consistent with the 2.2 and 6.2 km s^{-1} systematic uncertainties for the 1200 and 600 line mm^{-1} gratings, respectively. We find a median error of $\sigma_{tot} = 3.6$ km s^{-1} for stars in the And IX mask, and $\sigma_{tot} = 6.6$ km s^{-1} for the stars in the And XI, And XII and And XIII masks.
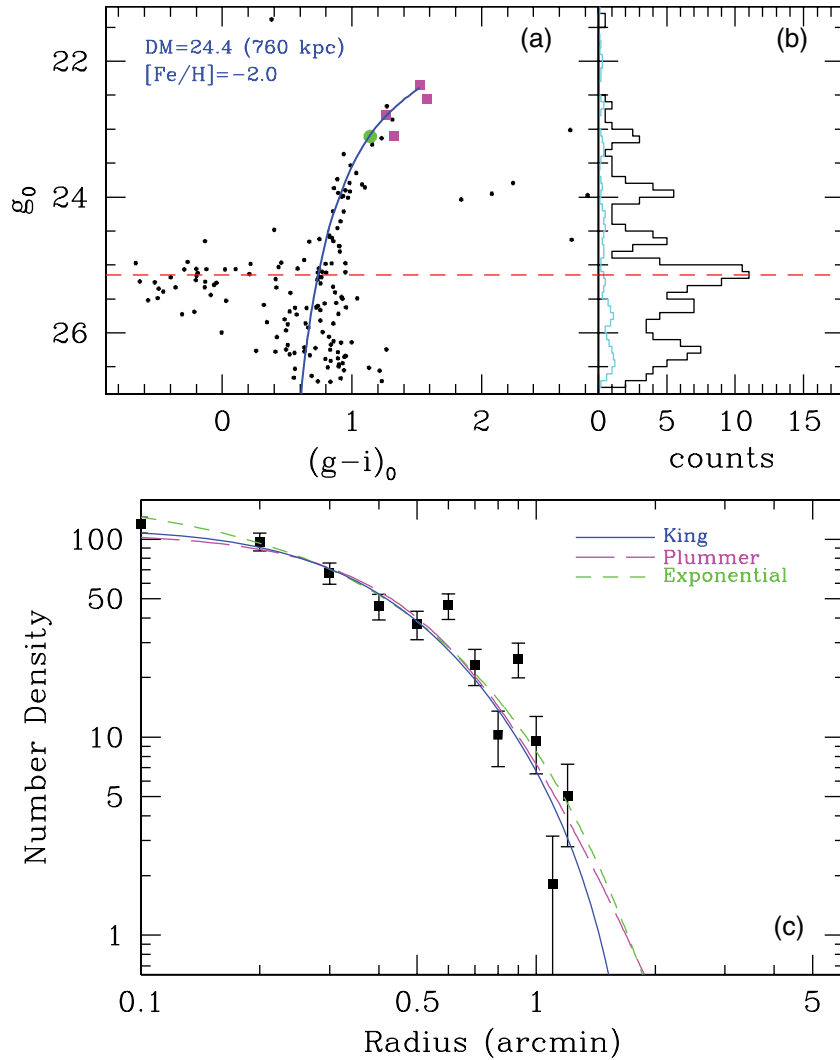
Figure 5. Top left: here we display the dereddened Subaru CMD for And XI and highlight the stars for which DEIMOS spectroscopy is available with magenta squares. The outlier at $-432.3\,\mathrm{km\,s^{-1}}$ is highlighted in green. A Dartmouth isochrone with $[\alpha/\mathrm{Fe}] = +0.4$, $[\mathrm{Fe/H}] = -2.0$ and age 13 Gyr (Dotter et al. 2008) is overlaid at a distance modulus of 24.5 (equivalent to 760 kpc) with $[\mathrm{Fe/H}] = -2.0$. Top right: the luminosity function for And XI in the g band is displayed as a histogram, and a clear peak at 25.1 for the HB is observed compared with the normalized luminosity function of a comparison region in the surrounding area of the dwarf (blue histogram). Bottom panel: the radial density plot for And XI with King (solid line), Plummer (long dashed line) and exponential (short dashed line) overlaid, with corresponding $r_{1/2} = 0.64 \pm 0.05$, 0.72 ± 0.06 and 0.71 ± 0.03 arcmin.

3 SATELLITE PROPERTIES

3.1 And XI

And XI is the most luminous of the three dSphs reported in Martin et al. (2006). The stars in the CFHT/MegaCam survey follow a well-defined RGB. The satellite lies at a projected distance of 106 kpc from M31 (assuming a distance of 785 kpc for M31). Below we present the structural and kinematic properties of this faint galaxy.

3.1.1 Photometric properties

First, we discuss the updated structural parameters derived for the And XI dwarf using the data from Subaru/Suprime-Cam. The extinction corrected and dereddened CMD for this data is shown in Fig. 5(a), containing only stars within a radius of 1.5 arcmin of the centre of And XI, defined as the mean of the positions of the stars

within 3 arcmin, giving $(\alpha, \delta) = (00^{\mathrm{h}}46^{\mathrm{m}}21^{\mathrm{s}}, +33°48'22'')$. The Subaru data probe much further down the luminosity function than the original CFHT data used by Martin et al. (2006) and shown in Fig. 1, and is complete down to the level of the HB at $g \sim 25$. To assess the half-light and tidal radii of And XI, we construct a background corrected radial surface density profile of And XI using circular annuli; this can be seen in Fig. 5(c). A background level of 8.1 ± 0.4 stars arcmin^{-2} was determined from a series of comparison regions in the area surrounding the dwarf. The half-light radius is then calculated by using a χ^2 fitting routine to apply King (with $r_{\mathrm{t}} = 2.23 \pm 0.2$ arcmin), Plummer and exponential profiles to the radial density data. For And XI this yields half-light radii $(r_{1/2})$ of 0.64 ± 0.15, 0.72 ± 0.06 and 0.71 ± 0.03 arcmin, respectively, with the exponential profile providing the best fit (with a reduced χ^2 of 2.6) to the data. Alternatively, applying the algorithm of Martin, de Jong & Rix (2008) produces a similar result of 0.68 ± 0.04 arcmin and converges on structural parameters without a strong ellipticity,

$\eta = 0.08$ (Martin, private communication), justifying the use of circular annuli in this case.

The CFHT data analysed by Martin et al. (2006) were not deep enough to measure the distance to And XI, however, our deeper, more complete Subaru observations allow us to place constraints on the distance to the satellite by combining the photometric data with our spectroscopic data (which we discuss in more depth below). One can define the apparent magnitude of the tip of the red giant branch (TRGB) for the dwarf by assuming that our brightest spectroscopically confirmed member represents the tip, allowing us to calculate the distance to the satellite. Using the brightest DEIMOS star (which has an apparent magnitude, $I_{0,\mathrm{Vega}} = 20.393$), and assuming the absolute magnitude of the TRGB is $M_{I_0,\mathrm{Vega}} = -4.04$ (Bellazzini et al. 2004), we find the maximum distance to be $D_{\max} = 770\,\mathrm{kpc}$. To determine the minimum distance, we must assess what the maximum possible offset could be from this brightest RGB star to the true TRGB. To do this, we follow the procedure of Chapman et al. (2007), analysing the well-populated RGB of the dSph, And II (McConnachie & Irwin 2006b). With 1000 random samples of four of the brightest stars from the top magnitude of the And II RGB, we constrain a probability distribution for the true TRGB, corresponding to a most likely offset of 0.5 mag. Using this value, we find the range of distances to And XI is 610–770 kpc. We note that this calculated range is based on assumption that the brightest DEIMOS star is found within 0.5 mag of the TRGB. While this seems reasonable, the distance range we calculate would vary if this assumption were changed. Therefore, as a sanity check for these values, we can also look for the peak in the luminosity function due to the HB of And XI in the luminosity function, shown in Fig. 5(b). An inspection of this reveals a clear peak at g-magnitude of $\sim$25.1 (red dashed line). Given that the absolute magnitude of the HB in the g band is $M_{\mathrm{HB}} = 0.6$ (Irwin et al. 2007) – though we note that this assumed value is sensitive to age and metallicity effects, see Chen, Zhao & Zhao 2009 for a discussion – we can estimate a distance modulus for the satellite of $\sim$24.5 (830 kpc), which sits outside of our calculated range for the satellite. This result demonstrates the difficulty in determining distances for faint satellites such as And XI. A companion paper, analysing *Hubble Space Telescope* (*HST*) data for And XI, And XII and And XIII (Martin et al., in preparation), will discuss the distances to these galaxies in more detail. For now, we use an intermediate distance of $760^{+70}_{-150}\,\mathrm{kpc}$ (where the upper and lower error bounds correspond to the maximum and minimum distances estimated within this work) for the remainder of our analysis.

In order to assess a mean photometric metallicity for the satellite, we use the Dartmouth isochrone models of Dotter et al. (2008), at a α element abundance of $[\alpha/\mathrm{Fe}] = +0.4$ and an age of 13 Gyr. We use $[\alpha/\mathrm{Fe}] = +0.4$ as it has been shown in numerous studies (e.g. Marcolini et al. 2008), that the α abundance for metal-poor stars in dSph populations such as those studied herein, tend to scatter between $[\alpha/\mathrm{Fe}] = +0.2$ and $+0.5$. We overlay isochrones at distances of 610, 830 and 760 kpc (corresponding to the upper, lower and HB distances calculated above), and note the best-observed fit in each case. This gives a metallicity range of $[\mathrm{Fe}/\mathrm{H}] = -1.5$ to -2.0 for the dwarf. In Fig. 5, we overlay the isochrone corresponding to the best-observed fit at 760 kpc ($[\mathrm{Fe}/\mathrm{H}] = -2.0$). We note that using a less α-enhanced isochrone model (with $[\alpha/\mathrm{Fe}] = +0.2$), gives a slightly more metal-rich value, with a best-observed fit at the HB distance of $[\mathrm{Fe}/\mathrm{H}] = -1.9$.

We use the Subaru data to recalculate the luminosity of the satellite by summing the flux of the likely member stars lying on the RGB and HB in the CMD of the satellite. By summing the flux of stars populating the CMD of the well studied globular cluster M92[1] within its half-light radius ($r_{1/2} = 19.6\,\mathrm{arcsec}$; Ferraro et al. 2000), using archival *HST* data, we calculate the total flux contained in this radius from the TRGB down to the HB. As our own data start come incomplete at roughly the HB level, we calculate a range for the contained flux by choosing two different cuts for the HB of M92. We find that 58–68 per cent of the total luminosity of the satellite is contained within this region, and we calculate a value for the total luminosity of And XI of $4.9^{+0.4}_{-0.2} \times 10^4\,\mathrm{L}_\odot$. Using the revised distance estimate above and this luminosity, we update the derived parameters of And XI, with the half-light radius, $r_{1/2}$, becoming $145^{+15}_{-29}\,\mathrm{pc}$ using the half-light radius from the exponential profile (previously estimated as 115 pc), and $M_v = -6.9^{+0.1}_{-0.5}$, in agreement with the findings of Martin et al. (2006).

3.1.2 Spectroscopic properties

Here we present the spectroscopic results from And XI; the data for each spectroscopic member star can be found in Table 2. Of the stars that were identified as potential And XI members from the CFHT CMD and targeted with DEIMOS, four appear to be kinematically associated with the satellite. As shown in the top left-hand panel of Fig. 6, where we outline the spectroscopic results for And XI, one can clearly identify a kinematic peak lying at a heliocentric velocity of $\sim -420\,\mathrm{km\,s^{-1}}$. These four stars have a mean velocity of $v_r = -419.4\,\mathrm{km\,s^{-1}}$ and an unusually low dispersion of $\sigma_v = 2.4\,\mathrm{km\,s^{-1}}$ (which we note is uncorrected for instrumental errors). We also initially identify one other star as a potential member of And XI with a velocity of $-432.3\,\mathrm{km\,s^{-1}}$. While it is clearly an outlier in velocity, it is important to assess its potential membership to the satellite. The inclusion of this star as a member increases the uncorrected values of v_r to $-422\,\mathrm{km\,s^{-1}}$ and σ_v to $4.0\,\mathrm{km\,s^{-1}}$, however, the velocity error on this fifth star is greater than the other four candidate members ($10.8\,\mathrm{km\,s^{-1}}$ versus average v_{err} of $6.2\,\mathrm{km\,s^{-1}}$). This is partially due to the fact that the Ca II_{8662} line is completely buried in the noise of the spectrum, as shown in the bottom right-hand panel of Fig. 6. As a result, when cross-correlating the spectrum with the Ca II template we achieve a peak in the correlation function of less than 0.1 and a TDR value of only 3.4, implying that our velocity measurement for this star is unreliable. For this reason, we define this star as a tentative member of And XI, but we exclude it from the following kinematic analysis.

It is important for us to determine whether any of our remaining stars are contaminants in the form of either foreground G dwarf stars or M31 halo stars. Because And XI has such a highly negative velocity ($\sim -420\,\mathrm{km\,s^{-1}}$), contamination from MW G dwarfs is unlikely, as these are predominantly found at velocities of greater than $-160\,\mathrm{km\,s^{-1}}$ (Robin et al. 2004; Ibata et al. 2005), so the chances of us finding these stars at the velocity of And XI are slim. Nevertheless, we can make use of the Na I doublet, a pressure sensitive absorption feature observed at $\sim$8100 Å. The strength of this feature is strongly correlated with the surface gravity of stars, therefore, it is prominent in G dwarfs, and much weaker in RGB stars. As our spectra cover the region of this doublet, we can measure the equivalent widths (EWs) of the lines. Any star for which the EW of the Na I doublet is greater than 1.8 Å we classify as a foreground contami-

---

[1] We use M92 as a comparison, rather than another M31 dSph as its CMD is well populated past the HB level, allowing us to better estimate the fraction of luminosity contained within this region. In addition, the satellites studied in this paper all appear to be relatively old, making the comparison with a globular cluster reasonable.
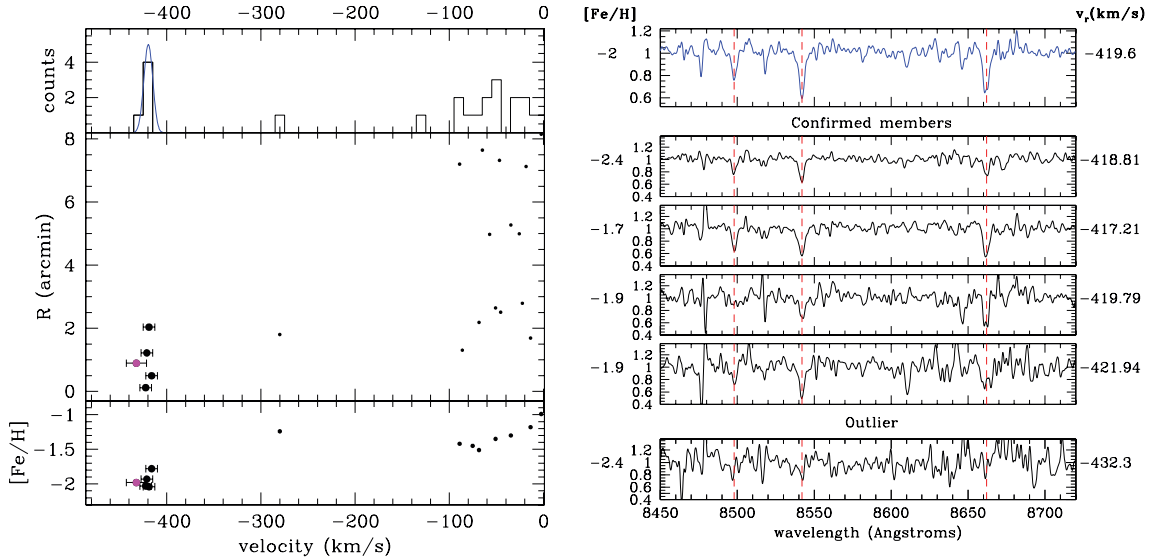
Figure 6. Left-hand panel: the velocities of observed stars in the And XI field are shown as a histogram, with the five candidate And XI member stars (seen as a kinematic grouping at approximately $-420\,\mathrm{km\,s^{-1}}$) highlighted as a heavy histogram. To differentiate And XI stars from the field, we additionally plot the velocities against their radius from the And XI centre, and in the lower panel, we display their photometric metallicities as a function of radial velocity, which were derived by interpolating between Dartmouth isochrones (Dotter et al. 2008) with $[\alpha/\mathrm{Fe}] = +0.4$ and age = 13 Gyr. Right-hand panel: the normalized spectra for each of the four plausible member stars of And XI and the outlier (bottom spectrum) are shown, with the combined spectrum of the four plausible members plotted in the top panel. The spectroscopic [Fe/H] for each candidate member is shown also, and we derive $[\mathrm{Fe/H}] = -2.0 \pm 0.2$ from the composite spectrum.

nant. As there is some overlap in the EWs of these two populations, this will inevitably lead to the occasional misclassification, but it should ensure that the majority of foreground stars are removed. For the four stars we classify as members of And XI we measure the EW of the Na I doublet to be less than 1.5 Å in all cases. Contaminating M31 halo stars are more difficult to cleanly define. The M31 halo has a systemic velocity of $\sim -300\,\mathrm{km\,s^{-1}}$ and an average dispersion of $\sim 90\,\mathrm{km\,s^{-1}}$, (Chapman et al. 2006; Kalirai et al. 2006) so it is possible that stray halo stars in the tails of the distribution could be found at a velocity similar to that of And XI. However, given the position of And XI, found in a low-density region of M31's halo, finding such a star within a few half-light radii of the object is unlikely. To limit any such contamination, we impose a radial cut on our members, requiring them to sit within the tidal radius of the dSph, 2.13 arcmin. We plot the distance of all observed stars from the centre of And XI as a function of their velocity in Fig. 6. It can be seen that all our candidate members lie within this radius. As a final check for contaminants, we plot the photometric metallicity of each star as a function of velocity, derived by interpolating between the same Dartmouth isochrones (Dotter et al. 2008) as used in Section 3.1.1. Halo stars are expected to have metallicities of $[\mathrm{Fe/H}] \sim -1.4$, and foreground dwarfs analysed with these isochrones would likely appear to have metal-rich metallicities of $[\mathrm{Fe/H}] \sim -0.6$. Our four member stars and the outlier are all found to be similarly metal poor, with a median $[\mathrm{Fe/H}] = -1.9$. Combining these factors, we find no reason to reject any of our four plausible members as contaminants.

The spectra for each of the candidates (including the outlier) are displayed in Fig. 6, along with a composite spectrum for the four most plausible members (weighted by their S/N), which is shown in the top right-hand panel, highlighted in blue. As each of the spectra has a high enough S/N, we can determine their metallicity individually and also calculate an average value from their sum, from the Ca II triplet (as described in Ibata et al. 2005), giving a

resulting measure of [Fe/H] for the satellite which is independent of photometric calculations. This relation between the EWs of the Ca II triplet and the resulting metallicity is dependent on the absolute V-band magnitude of the observed star. By summing together stars of different magnitudes we introduce an error into our calculations as we must assume an average value for the V-band magnitude of our sample. As the stars analysed within this work are all of a similar luminosity, this error is typically small (less than 0.1 dex), and we factor this into our error calculations. The average value determined from the combined spectrum is $[\mathrm{Fe/H}] = -2.0 \pm 0.2$. This is considerably more metal poor than that calculated by Martin et al. (2006) of $[\mathrm{Fe/H}] = -1.3$ from the CFHT photometry. This is likely due to the use of Girardi et al. (2004) isochrones in their study, which produce more metal-rich values in the MegaCam filter sets than other isochrone models, such as the Dotter isochrones used in this paper. This effect has been noted in the globular clusters NGC 2419 and M92 (Girardi et al. 2004, 2008), where the Girardi et al. isochrone models in the $g - i$ colours produce more metal-rich values for these objects than other published values.

Following the maximum likelihood algorithm outlined in Martin et al. (2007), we calculate the mean radial velocity, v_r, and the intrinsic velocity dispersion, σ, for And XI by sampling a coarse grid in (v_r, σ) space and determining the parameter values that maximize the likelihood function (ML), defined as

$$\mathrm{ML}(v_r, \sigma) = \prod_{i=1}^{N} \frac{1}{\sigma_{\mathrm{tot}}} \exp\left[-\frac{1}{2} \left(\frac{v_r - v_{r,i}}{\sigma_{\mathrm{tot}}} \right)^2 \right], \qquad (1)$$

with N the number of stars in the sample, $v_{r,i}$ the radial velocity measured for the ith star, $v_{\mathrm{err},i}$ the corresponding uncertainty and $\sigma_{\mathrm{tot}} = \sqrt{\sigma^2 + v_{\mathrm{err},i}^2}$. In this way, we are able to separate the intrinsic dispersion of And XI from the dispersion introduced by our measurement uncertainties. We display the one-dimensional likelihood distributions for v_r and σ_v in Fig. 7 where the
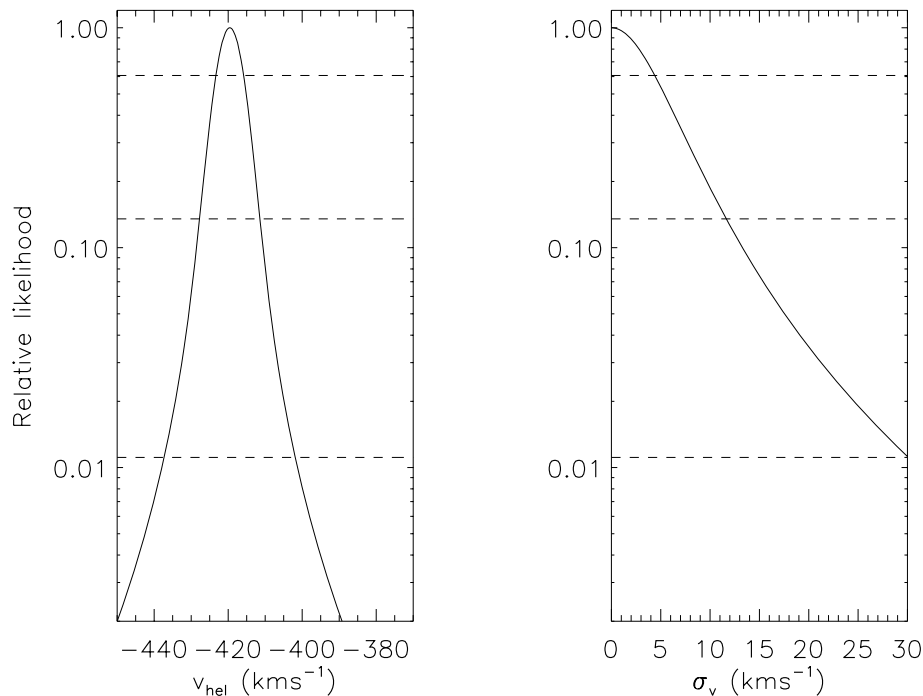
Figure 7. Likelihood distributions of member stars in And XI, showing the most likely values of radial velocity (left-hand panel) and velocity dispersion (right-hand panel) for our four confirmed members. The dashed lines indicate the 1σ, 2σ and 3σ uncertainties. The most-likely velocity for And XI is $v_{\mathrm{r}} = -419.6\,\mathrm{km\,s^{-1}}$ and the dispersion is not quite resolved. We use the value of $4.6\,\mathrm{km\,s^{-1}}$ from the 1σ confidence level as an upper limit for the dispersion of And XI.

dashed lines represent the conventional 1σ, 2σ and 3σ (68, 95 and 99.7 per cent) uncertainties on the values. We recover a systemic velocity for And XI of $v_{\mathrm{r}} = -419.6^{+4.4}_{-3.8}\,\mathrm{km\,s^{-1}}$ (where the errors indicate the 1σ uncertainties). Owing to our low sample size and S/N, the dispersion is unresolved, however, the 1σ value suggests a maximum value of $4.6\,\mathrm{km\,s^{-1}}$ from the data, which we overlay as a Gaussian curve in the top panel of Fig. 6(a). We note that these values are only marginally affected if we include the tentative member at $-432.3\,\mathrm{km\,s^{-1}}$, with v_{r} increasing to $-422.5\,\mathrm{km\,s^{-1}}$, and σ_v is still unresolved at $0\,\mathrm{km\,s^{-1}}$, with a maximum set by the 1σ uncertainty of $\sim 5\,\mathrm{km\,s^{-1}}$.

These results suggest that the velocity dispersion of And XI is unusually low, comparable to the curious MW objects Willman 1 and Leo V, which have measured dispersions of $4.2^{+2.1}_{-1.1}$ and $2.4^{+2.4}_{-1.4}\,\mathrm{km\,s^{-1}}$, respectively (Martin et al. 2007; Walker et al. 2009a), and the M31 dSph, And X, which has a dispersion of $3.9 \pm 1.2\,\mathrm{km\,s^{-1}}$ (Kalirai et al. 2009). We caution that the calculation of dispersions for cold systems such as And XI rely heavily on accurately knowing the errors attributed to each velocity measurement. Whilst we have attempted to investigate our errors as thoroughly as possible (as detailed in Section 2.2.1), if we have overestimated our errors, we will have underestimated our velocity dispersion (and vice versa), and the true velocity dispersion could be higher than the dispersion we calculate here.

Using the spectral data obtained above, we can make an estimate for the mass of And XI by assuming it is a spherical system in virial equilibrium. Throughout the literature, several different methods for calculating the mass of dispersion-supported galaxies – such as And XI – are employed which do not necessarily produce similar values when applied to the same data sets. This makes comparisons of these values for Local Group dSphs difficult, as one is not necessarily comparing like with like. In this work, we shall use three

different methods to estimate the mass of our dSphs; the Richstone & Tremaine (1986) and Illingworth (1976) methods, which are the two most common approaches, and we also apply a new method, presented in Walker et al. (2009b), which we discuss in more detail below.

First, we apply the core-fitting method of Richstone & Tremaine (1986). This method assumes that the system is in virial equilibrium with a flat core, an isotropic velocity distribution and a constant M/L throughout. One can then derive the M/L of And XI from

$$M/L = \eta \frac{9}{2\pi G} \frac{\sigma_0^2}{S_0 r_{\mathrm{hb}}}, \qquad (2)$$

where S_0 is the central surface brightness of the dwarf, r_{hb} is the value of the radius where the surface brightness drops to half the peak surface brightness (approximately $2/3 \times r_{1/2}$) and σ_0 its central velocity dispersion. η is a model-dependent, dimensionless constant that Richstone & Tremaine (1986) showed to be very nearly unity for a wide range of mass models, e.g. the isothermal sphere, where they found $\eta = 1.013$. For And XI, we derive $S_0 = 0.455 \pm 0.09\,\mathrm{L_\odot\,pc^{-2}}$ when using $\mu_v = 27.35\,\mathrm{mag\,arcsec^{-2}}$, and taking $r_{1/2} = 145^{+15}_{-19}\,\mathrm{pc}$ we find $r_{\mathrm{hb}} = 97^{+10}_{-19}\,\mathrm{pc}$. We further assume $\sigma_0 = \sigma_v = 4.7\,\mathrm{km\,s^{-1}}$ (taking the 1σ limit from our maximum likelihood calculation) and use this to derive an effective upper limit on the M/L for And XI. This leads to $(M/L) < 152\,\mathrm{M_\odot/L_\odot}$. Combining this with the updated luminosity of $4.9^{+0.4}_{-0.2} \times 10^4\,\mathrm{L_\odot}$ calculated above, we deduce an upper limit on the mass of And XI of $M < 7.4 \times 10^6\,\mathrm{M_\odot}$.

The prescription of Illingworth (1976), uses an $r^{1/4}$ law to describe the surface brightness profile of the system, rather than the core-fitting technique of Richstone & Tremaine (1986). It again assumes virial equilibrium and an isotropic velocity distribution for

the system. One can then derive the mass using

$$M = \eta r_{1/2} \sigma_v^2, \tag{3}$$

where $\eta = 850 \, M_\odot \, pc^{-1} \, km^{-2} \, s^2$, we calculate $M < 2.6 \times 10^6 \, M_\odot$ and $M/L = 53$, which is less than half the value derived above, highlighting the difficulty faced in comparing the masses of dSphs within the Local Group.

Recently, papers by Walker et al. (2009b) and Wolf et al. (2010) have shown that the mass within the half-light radius of dispersion-supported galaxies, such as dSphs, can be accurately estimated with only mild assumptions about the spatial variation of the stellar velocity dispersion anisotropy (β), giving it an advantage over other methods (such as those described above), which are more sensitive to the adopted value of β. Following the approach of Walker et al. (2009b), we can derive the mass contained within $r_{1/2}$ (M_{half}) from

$$M_{\mathrm{half}} = \mu r_{1/2} \sigma_v^2, \tag{4}$$

where $\mu = 580 \, M_\odot \, pc^{-1} \, km^{-2} \, s^2$. For And XI, this gives us an upper limit on M_{half} for the dSph of $1.7 \times 10^6 \, M_\odot$. We do note that, as two of our four And XI members sit outside of the half-light radius for the dwarf, we are assuming that there is no variation of σ_v with radius, which may not be the case. This could cause us to underestimate the mass of And XI within this region.

3.2 And XII

And XII was the faintest of the trio of dwarfs presented in Martin et al. (2006), with an absolute magnitude of $M_v = -6.4$. Its orbital properties were discussed in a previous paper by Chapman et al. (2007), where it was shown that due to its large radial velocity, it was likely only experiencing the gravitational effects of M31 for the first time. In this section, we give a complete overview of the photometric and spectroscopic properties of And XII in the same format as for And XI. We list the properties of our spectroscopically confirmed members in Table 3.

3.2.1 Photometric properties

First, we discuss the structural properties derived for And XII from the Subaru data. We determine the centre of And XII as $(\alpha, \delta) = (00^h 47^m 27^s, +34° 22' 29'')$ using the same technique as for And XI, and we display the Subaru CMD for all stars within a 1.5-arcmin radius of the centre of And XII in Fig. 8(a) (pink squares represent the DEIMOS candidate members in this data set). The background-corrected radial profile can be seen in Fig. 8(c), with a background level of 9.9 ± 0.4 stars arcmin^{-2}. Plummer and exponential models were fitted and are shown overplotted on the data. The Plummer and exponential fits yield half-light radii of 1.2 ± 0.2 and 1.1 ± 0.2 arcmin, respectively, with the plummer profile showing the best fit to the data (reduced χ^2 of 3.7 versus 3.9). The King profile would not converge on a physical fit for these data, yielding results where the tidal radius is over an order of magnitude smaller than the half-light radius. We therefore fit a King profile, with the half-light radius fixed to the half-light radius given by the Plummer profile. The resulting best-fitting tidal radius is $r_t = 3.1 \pm 0.3$ arcmin, and we use this value as a cut for membership in Section 3.2.2. As can be seen in Fig. 8, the radial profile for And XII is not as clean as for And XI, and this may be due to the presence of variable extinction in the field of And XII, which appears (based on visible cirrus) to vary on angular scales of ~ 1 arcmin, and is reflected by

the larger errors in $r_{1/2}$ (of order ~ 10–20 per cent compared with ~ 5 per cent for And XI) and the inability to successfully fit a King profile to the data. This small-scale extinction is also present in a nearby globular cluster, MGC1 (Mackey et al. 2010), and is found to vary on scales much smaller than the 6×6 arcmin^2 resolution of the Schlegel et al. (1998) dust maps of this region. Conversely, these poor fits could be indicative of tidal disruption in the outer regions of And XII; however, given the large systemic velocity of -558.4 km s^{-1} (discussed in Section 3.2.2), this is unlikely to have been as a result of an interaction between And XII and M31, as And XII is likely experiencing the potential of its host for the first time (Chapman et al. 2007).

Adopting the same TRGB Monte Carlo procedure as with And XI we find $D_{\mathrm{max}} = 1$ Mpc, and assuming a maximum offset of 0.5 mag from the true TRGB, we compute a range of distances to And XII of 800–1000 kpc, consistent with the most likely distance for And XII of 830 ± 50 kpc found by Chapman et al. (2007). An inspection of the luminosity function of And XII shown in the top right-hand panel of Fig. 8(b) reveals a clear peak in the HB at g-magnitude just below ~ 25.3, implying a distance modulus for the satellite of $\mu \sim 24.7$ (870 kpc), which sits within our calculated range. We use the most-likely distance of 830^{+170}_{-30} kpc from Chapman et al. (2007) for the remainder of our analysis. Again, we recalculate the luminosity of the satellite, finding a value of $L = 3.1^{+0.2}_{-0.1} \times 10^4 \, L_\odot$, corresponding to an absolute magnitude of $M_v = -6.4^{+0.1}_{-0.5}$ and a half-light radius (using the value from the exponential model), $r_{1/2}$, becomes 289^{+67}_{-49} pc (previously estimated as 125 pc).

We analyse the CMD of And XII to ascertain a mean value of [Fe/H] for the dSph. We overlay Dotter et al. (2008) isochrones (with age and abundance as detailed in Section 3.1.1) for the range of distances calculated for And XII above (800–1000 kpc), and conclude that the metallicity of And XII lies between [Fe/H] = -1.7 and [Fe/H] = -2.0. In Fig. 8 we overlay the best-observed fit for the most-likely distance (830 kpc), with [Fe/H] = -1.9.

3.2.2 Spectroscopic properties

We now discuss the kinematic results for And XII. As seen in Fig. 9, eight stars are found to be kinematically associated with And XII at a velocity of ~ -560 km s^{-1}. Unlike And XI we have no ambiguity about which of these stars are members as they are tightly distributed in velocity, all sit within 2 arcmin ($< 2r_{1/2}$) of the dwarf centre, and all show negligible absorption at the position of the Na I doublet. Their photometric metallicities (lower left-hand panel of Fig. 9) are also in good agreement with one another, ranging from [Fe/H] = -1.7 to -2.3, with median [Fe/H] = -1.7. We display the individual spectra for each candidate member in Fig. 9, with the combined spectrum for the satellite shown in the top panel. Using the Ca II approach as described for And XI, metallicity measurements are made for each of the candidate stars, spanning [Fe/H] = -1.5 to -2.5, with a median [Fe/H] = -2.0. To estimate an average metallicity for the dwarf, we analyse the composite spectrum, and deduce a metallicity of [Fe/H] = -2.1 ± 0.2. Eliminating the three stars with poor S/N (bottom three panels of Fig. 9) yields a value of [Fe/H] = -2.0 ± 0.25. Both of these values agree well with the photometric metallicities discussed above.

Before correcting for measurement errors, the eight stars imply $\sigma_v = 4.9$ km s^{-1}. The same maximum likelihood approach as with And XI (the results of which are displayed in Fig. 10) yields a systemic velocity for the satellite of $-558.4^{+3.2}_{-3.2}$ km s^{-1}, and we (marginally) resolve a velocity dispersion for the satellite of
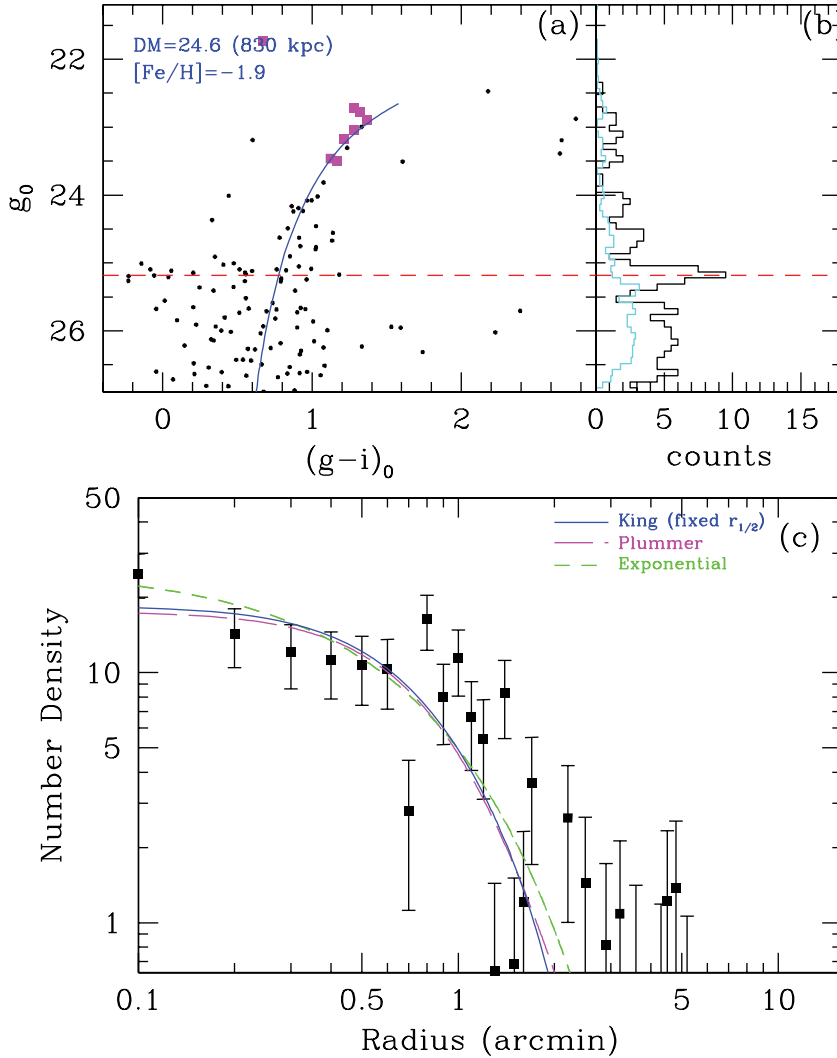
Figure 8. As Fig. 5 but for And XII. A Dartmouth isochrone is overplotted with [Fe/H] = −1.9 and [α/Fe] = +0.4 at distance modulus of 24.6 (830 kpc). In plot (c) Plummer and exponential profiles are overlaid, with respective half-light radii of 1.2 ± 0.2 and 1.1 ± 0.2 arcmin, with the exponential profile providing the best fit to the data. A King profile (with $r_{1/2}$ fixed at 1.2 arcmin) is overplotted also.

$\sigma_v = 2.6^{+5.1}_{-2.6}$ km s^{-1}, where the errors represent the 1σ uncertainties. Again, this value is uncommonly low for a dSph.

As before, we apply equations (2)–(4) to our And XII data in an attempt to constrain the mass and dark matter content of the galaxy. Using the Richstone & Tremaine (1986) equation for *M/L* (equation 2) and our updated parameters for $r_{1/2}$ of 289^{+67}_{-49} pc, $S_0 = 0.21^{+0.07}_{-0.05}$ L$_\odot$ pc^{-2} and the dispersion value from the maximum likelihood analysis of $3.8^{+3.9}_{-3.8}$ km s^{-1}, we find $M/L = 55^{+107}_{-55}$ M$_\odot$/L$_\odot$, giving a mass estimate of $1.7^{+3.3}_{-1.7} \times 10^6$ M$_\odot$. Equation (3) (Illingworth 1976) gives us $M/L = 54^{+107}_{-55}$ and a mass of $1.7^{+3.3}_{-1.7} \times 10^6$ M$_\odot$, in agreement with the Richstone & Tremaine (1986) approach. In both cases, this value falls below the historical ∼10^7 M$_\odot$ mass threshold typically observed for brighter dwarfs, even when taking the large errors into account.

Finally, applying the same formula for the mass within the half-light radius of And XII as for And XI (equation 4; Walker et al. 2009b), we calculate $M_{half} = 1.1^{+2.1}_{-1.1} \times 10^6$ M$_\odot$. For And XII, six of our eight member stars lie within the half-light radius of the dSph, making our measured σ_v a reasonable approximation for the dispersion within $r_{1/2}$.

3.3 And XIII

Discovered by Martin et al. (2006), And XIII suffered some chance contamination with a background galaxy cluster, increasing the apparent contrast of this dwarf in the imagery. None the less, the apparent brightness of And XIII is similar to And XI after correction for this contamination. We present our observations of And XIII in the same format as the other M31 dwarfs, and list our spectroscopic members in Table 4.

3.3.1 Photometric properties

Using the same Subaru photometric data set as for And XI and And XII, we find the centre of And XIII as $(\alpha, \delta) = (00^h51^m 50^s, +33°00'43'')$ and in Fig. 11(a) we show the Subaru CMD for all stars within a 1.5-arcmin radius of the centre of And XIII (DEIMOS candidate members are highlighted with pink squares, while tentative members are highlighted by light blue squares). The background-corrected radial profile is displayed here also (panel c, with a background level of 11.2 ± 0.4 stars arcmin^{-2}). King (with $r_t = 2.8 \pm$
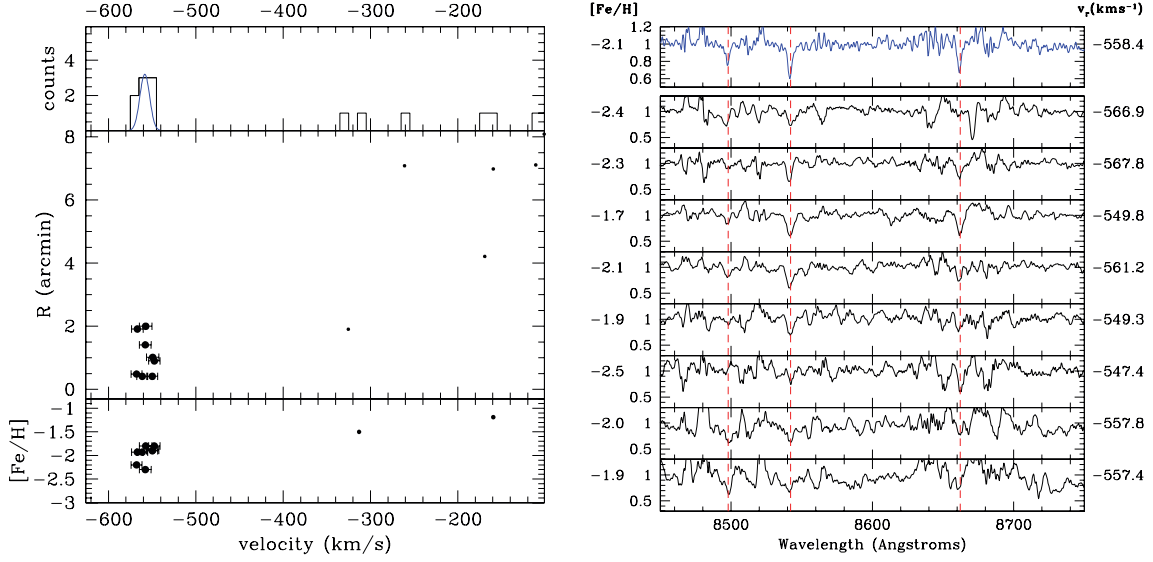
Figure 9. As Fig. 6, but for And XII. In the left-hand panel, And XII can be clearly identified as a kinematic grouping of eight stars at approximately −560 km s⁻¹, all located within 2 arcmin of the dwarf centre. The individual stars are all found to be metal poor, both photometrically (lower left-hand panel) and spectroscopically (right-hand panel). Analysis of the composite spectra of the confirmed members yields [Fe/H] = −2.1 ± 0.2.
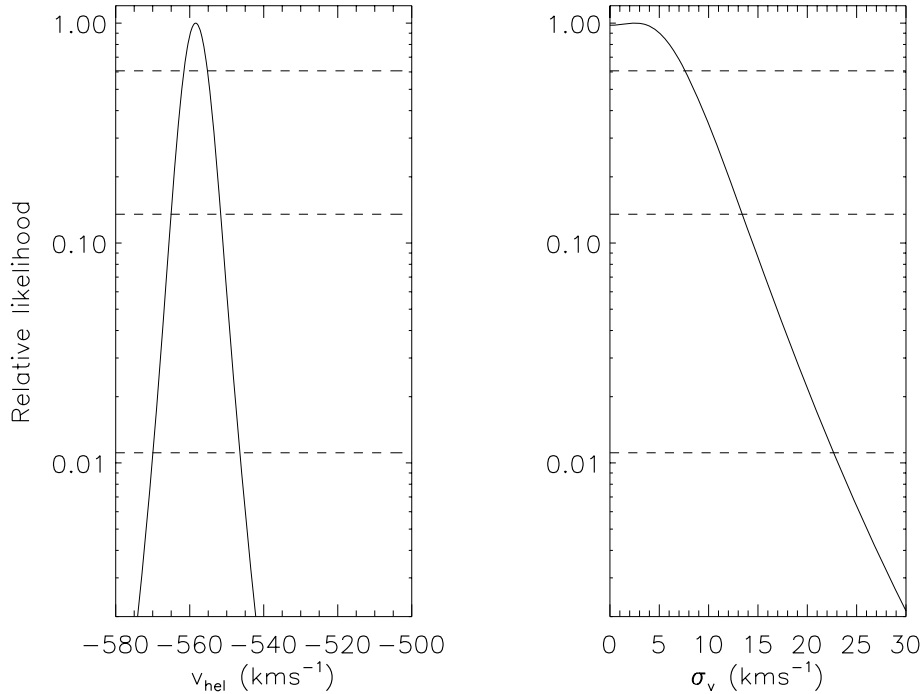

Figure 10. Likelihood distributions for And XII. Dashed lines represent the conventional 1σ, 2σ and 3σ confidence levels. The mean velocity for And XII is calculated to be −558.4 km s⁻¹, and we (marginally) resolve a velocity dispersion of $2.6^{+5.1}_{-2.6}$ km s⁻¹, though we note that this is consistent with zero within its 1σ uncertainties.

0.2), Plummer and exponential models are shown overplotted on the data. These yield half-light radii of 0.78 ± 0.08, 0.81 ± 0.09 and 0.66 ± 0.1 arcmin, respectively, with the King profile showing the best fit to the data. Again, this value of $r_{1/2}$ is consistent with the $r_{1/2}$ resulting from the application of the ML algorithm of Martin et al. (2008) (Martin, private communication).

Adopting the same TRGB Monte Carlo procedure as with the previous two dwarfs, we find $D_{max} = 940$ kpc for the satellite, and assuming a maximum offset of 0.5 mag from the TRGB, a range of distances of 750–940 kpc. We also find a distance modulus from

the HB of And XII of 24.8 (910 kpc), via inspection of the luminosity function, which is in good agreement with the results from the TRGB method. Using the HB distance, we calculate a total luminosity for the satellite of $L = 4.1^{+0.1}_{-0.2} \times 10^4$ L$_\odot$. These revised distance and luminosity values update the derived parameters of And XIII with M_v becoming $-6.7^{+0.4}_{-0.1}$ (previously estimated as −6.9), and the half-light radius, $r_{1/2}$, becomes 206^{+27}_{-44} pc (previously estimated as 115 pc).

As before, we overlay Dotter et al. (2008) isochrones (with age and abundance as detailed in Section 3.1) for the range of distances
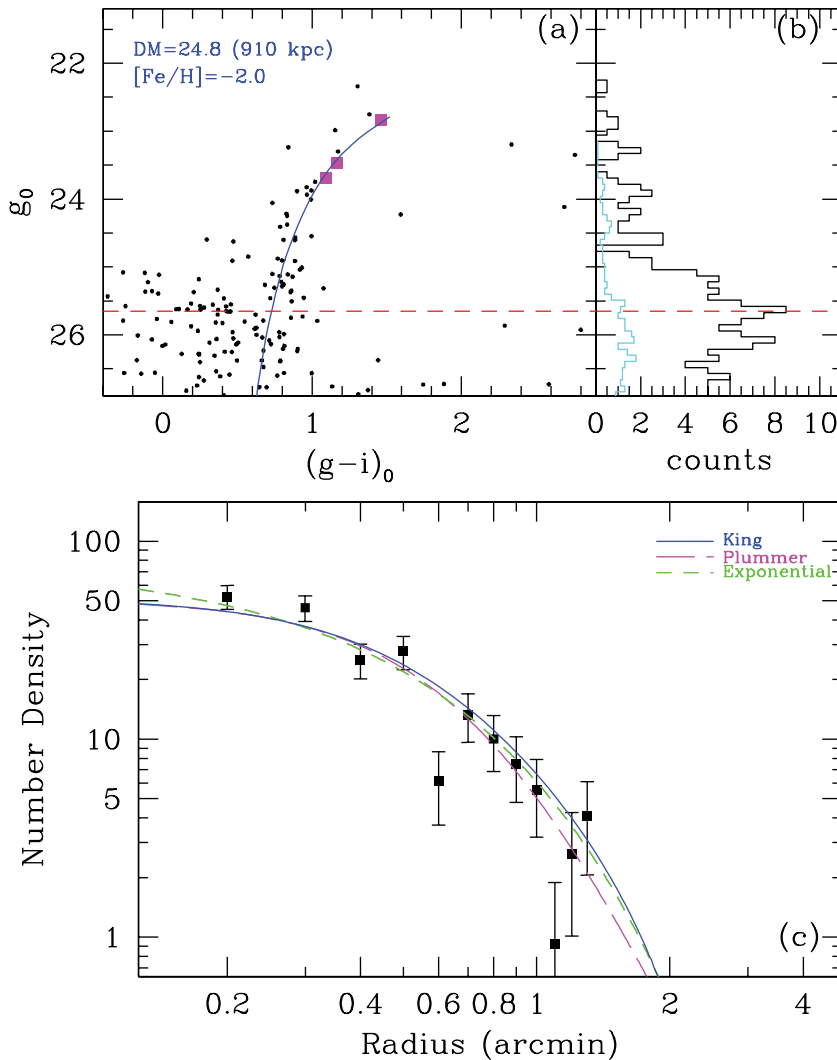
Figure 11. As Fig. 5 but for And XIII. Dartmouth isochrones (Dotter et al. 2008) is overlaid with [Fe/H] = −2.0 and [α/Fe] = +0.4 at the HB distance modulus of 24.8 (910 kpc as seen in the luminosity function of And XIII, plot b) In plot (c), King (with r_t = 2.8 arcmin), Plummer and exponential profiles are overlaid, with respective half-light radii of 0.78 ± 0.08, 0.81 ± 0.09 and 0.76 ± 0.1 arcmin, with the King profile providing the best fit to the data.

calculated for And XII above (750–940 kpc), giving a metallicity range of [Fe/H] = −1.8 to −2.1 for And XIII. In Fig. 11 we overlay the best-observed fit for the HB distance (910 kpc) which has [Fe/H] = −2.0.

3.3.2 Spectroscopic properties

Being the most distant of our four observed dSphs, And XIII has unsurprisingly provided us with the biggest challenge in identifying probable member stars. When examining the individual spectra for the stars in the And XIII mask (a sample of which can be seen in Fig. 12) we see that the Ca II$_{8662}$ line has experienced contamination from a skyline, which has significantly affected its profile. As a result, the EW of the third line, which should be ∼3/4 the EW of the second line, is larger than that of the second in most cases. Such an effect will obviously change the measured velocities and metallicities if we were to include it in our cross-correlations and metallicity calculations. For this reason, we derive velocities and metallicities for the satellite members based on the Ca II$_{8498}$ and Ca II$_{8542}$ lines only. The resulting kinematic data for And XIII are shown in Fig. 12. We can see that three RGB stars lying on the

Subaru CMD (Fig. 11) inhabit a similar region in velocity space, with an average $v_r \sim -190\,\mathrm{km\,s^{-1}}$. This implies that And XIII is currently moving away from M31. These three stars have an uncorrected dispersion of $\sigma_v = 4.3\,\mathrm{km\,s^{-1}}$. The systemic velocity of And XIII places it much closer to the regime of Galactic foreground contamination ($v_{hel} > -150\,\mathrm{km\,s^{-1}}$) than the previous two dwarfs. With this being the case, it is particularly important for us to assess whether any of our spectroscopic candidates could be contaminants. Measuring the EW of the Na I doublet in each star, we find that in each case the EW is significantly less than the 1.8 Å cut we defined in Section 3.1.2, making them unlikely foreground dwarf contaminants. To assess the likelihood of any of the three stars being M31 halo stars that happen to be coincident with And XIII we invoke a radial cut equal to the tidal radius (2.8 arcmin). All our potential member stars lie within this cut. Finally, we assess the quality of our derived velocities, and we note that all three stars have TDR >3.5, meaning that they satisfy our quality criteria. Therefore, we use all three potential members in our subsequent analysis. Using the summed spectrum of these members we calculate a metallicity for And XIII of [Fe/H] = −2.0 ± 0.3, which is again more metal poor than that of [Fe/H] = −1.4 reported in Martin et al. (2006),
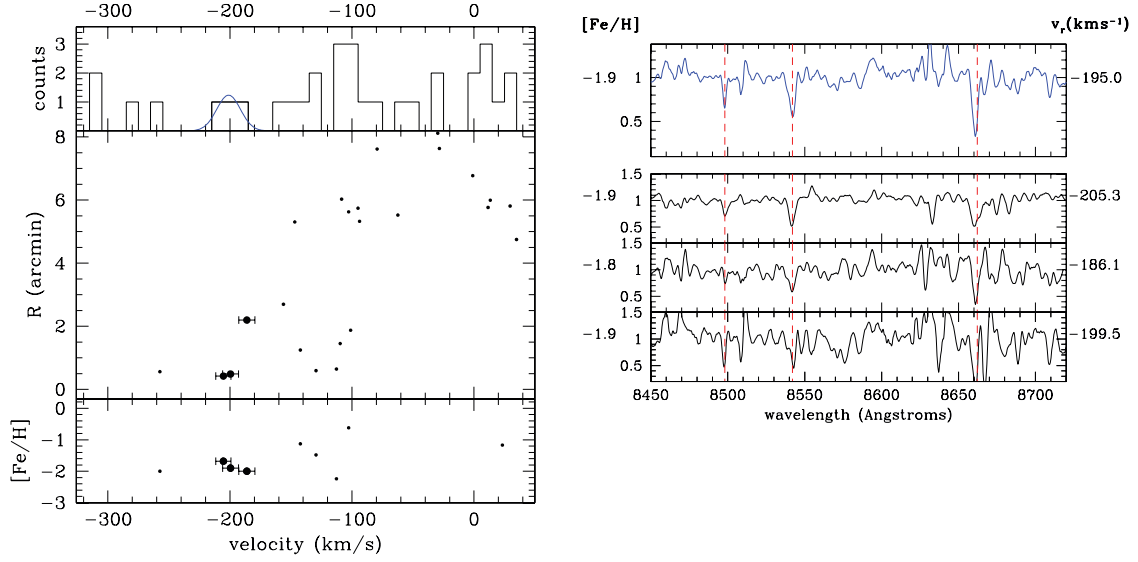
Figure 12. As Fig. 6, but for And XIII. In the left-hand panel, And XIII can be identified as a kinematic grouping of three stars at approximately $-200\,\mathrm{km\,s^{-1}}$, all of which are located within 2 arcmin of the dwarf centre. The individual stars are all found to be metal poor, both photometrically (lower left-hand panel) and spectroscopically (right-hand panel). Analysis of the composite spectra of the confirmed members yields [Fe/H] = -1.9 ± 0.2.

but in good agreement with our revised photometric metallicities detailed above.

The maximum likelihood distribution for the velocity and dispersion of And XIII is shown in Fig. 13. For our two probable members, the technique suggests $v_r = -195.0^{+7.4}_{-8.4}\,\mathrm{km\,s^{-1}}$ and a resolved dispersion of $\sigma_v = 9.7^{+8.9}_{-4.5}\,\mathrm{km\,s^{-1}}$. The corresponding errors are large ($\gtrsim 50$ per cent) owing to our small sample size (three stars) and the low S/N (9.9, 4.7 and 3.3 Å^{-1}) of our objects. If we compare this value with dispersions for MW objects of a comparable luminosity such as CVnI ($\sigma_v = 7.9\,\mathrm{km\,s^{-1}}$, $M_V = -7.1$; Simon & Geha 2007;

Martin et al. 2008) and Bootes I ($\sigma_v = 6.5\,\mathrm{km\,s^{-1}}$, $M_V = -6.3$; Martin et al. 2007, 2008), we find that the dispersion of And XIII is consistent with its counterparts within its 1σ errors.

We combine these results with the structural properties of And XIII derived from the Subaru data, to place a constraint the dark matter content of And XIII, using the same approach as for the previous dwarfs. Using equation (2) and a central surface brightness of $S_0 = 0.276^{+0.05}_{-0.08}\,\mathrm{L_\odot\,pc^{-2}}$ and the dispersion from our maximum likelihood analysis of $\sigma_v = 9.7\,\mathrm{km\,s^{-1}}$, we calculate a mass to light ratio of $M/L = 821^{+1065}_{-538}\,\mathrm{M_\odot/L_\odot}$ which implies a high dark
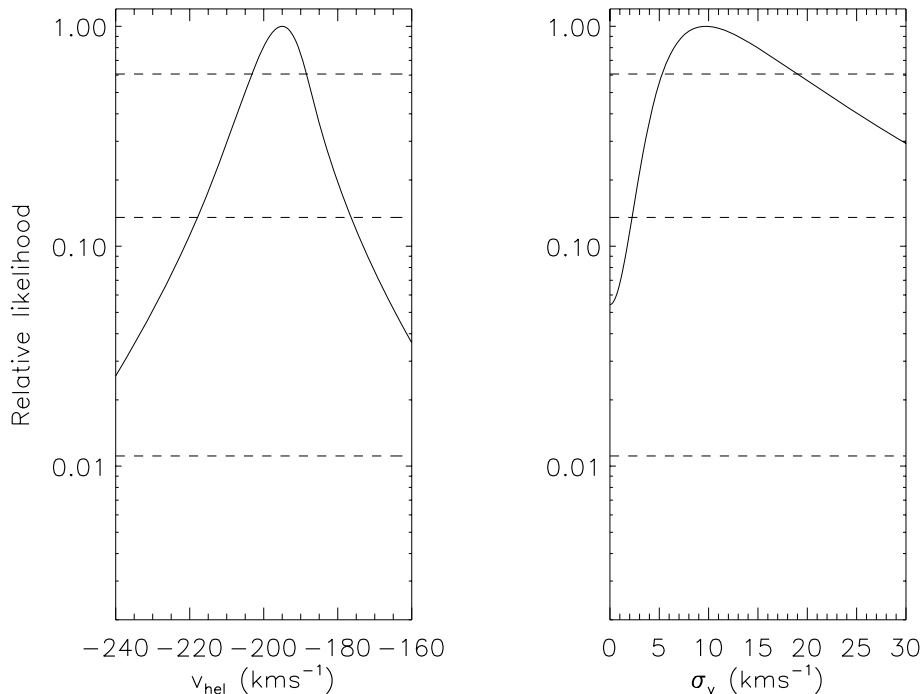

Figure 13. Likelihood distributions for And XIII. Dashed lines represent the conventional 1σ, 2σ and 3σ confidence levels. The mean velocity for And XIII is determined to be $-195.0\,\mathrm{km\,s^{-1}}$, and the velocity dispersion is resolved as $\sigma_v = 9.7^{+8.9}_{-4.5}\,\mathrm{km\,s^{-1}}$.

matter dominance. The upper limit for the mass is therefore $3.4^{+4.4}_{-2.2} \times 10^7 \, M_\odot$. The formula of Illingworth (1976) (equation 3) produces an upper limit on the mass of And XIII of $1.6^{+2.2}_{-1.0} \times 10^7 \, M_\odot$ (corresponding to $M/L = 390^{+505}_{-252}$), which is less than half the value derived using the method of Richstone & Tremaine (1986), as was the case for And XI. Applying the formula for M_{half} as before, we find $M_{\mathrm{half}} = 1.1^{+1.4}_{-0.7} \times 10^7 \, M_\odot$.

3.4 And IX

First reported by the SDSS team in Zucker et al. (2004), And IX has previously been studied both photometrically (Zucker et al. 2004; Harbeck et al. 2005; McConnachie et al. 2005a) and spectroscopically (Chapman et al. 2005). In this work we intend to expand on previous results by including new Subaru photometry [extinction corrected as for the previous dwarfs, with $E(B - V) = 0.08$ from the Schlegel et al. (1998) maps], and update the kinematic results obtained with DEIMOS in Chapman et al. (2005), having corrected for the error in the initial geometric models as discussed in Section 2. We present our observations of And IX in the same format as the other M31 dwarfs, and list all observed stars in Table 5.

3.4.1 Photometric properties

Using the Subaru data for the satellite, the centre of And IX is derived as $(\alpha, \delta) = (00^{\mathrm{h}}52^{\mathrm{m}}51\overset{s}{.}1, \, +43°11'48\overset{''}{.}6)$ using the same technique as for the previous dSphs. In Fig. 14(a) we show the Subaru CMD for all stars within a 2.5-arcmin radius of the centre of And IX (pink squares represent the DEIMOS candidate members in this data set). The background-corrected radial profile was calculated using circular annuli centred on these coordinates and can be seen in Fig. 14 (with a background level of 23 ± 4.8 stars arcmin^{-2}). King (with $r_{\mathrm{t}} = 6.6 \pm 0.3$ arcmin), Plummer and exponential models have been plotted over the data. These yield half-light radii of 2.7 ± 0.2, 2.6 ± 0.1 and 2.5 ± 0.1 arcmin, respectively, with the exponential profile showing the best fit to the data (reduced χ^2 of 1.8 versus 1.9 and 2.0 for King and Plummer profiles). Again, this is consistent with the results of the ML algorithm of Martin et al. (2008) (N. Martin, private communication).

Adopting the same TRGB Monte Carlo procedure as with And XI, we find $D_{\mathrm{max}} = 770$ kpc for the satellite, and we calculate a range of distances of 615–770 kpc for the dwarf. From the luminosity function, we infer a distance modulus based on the HB
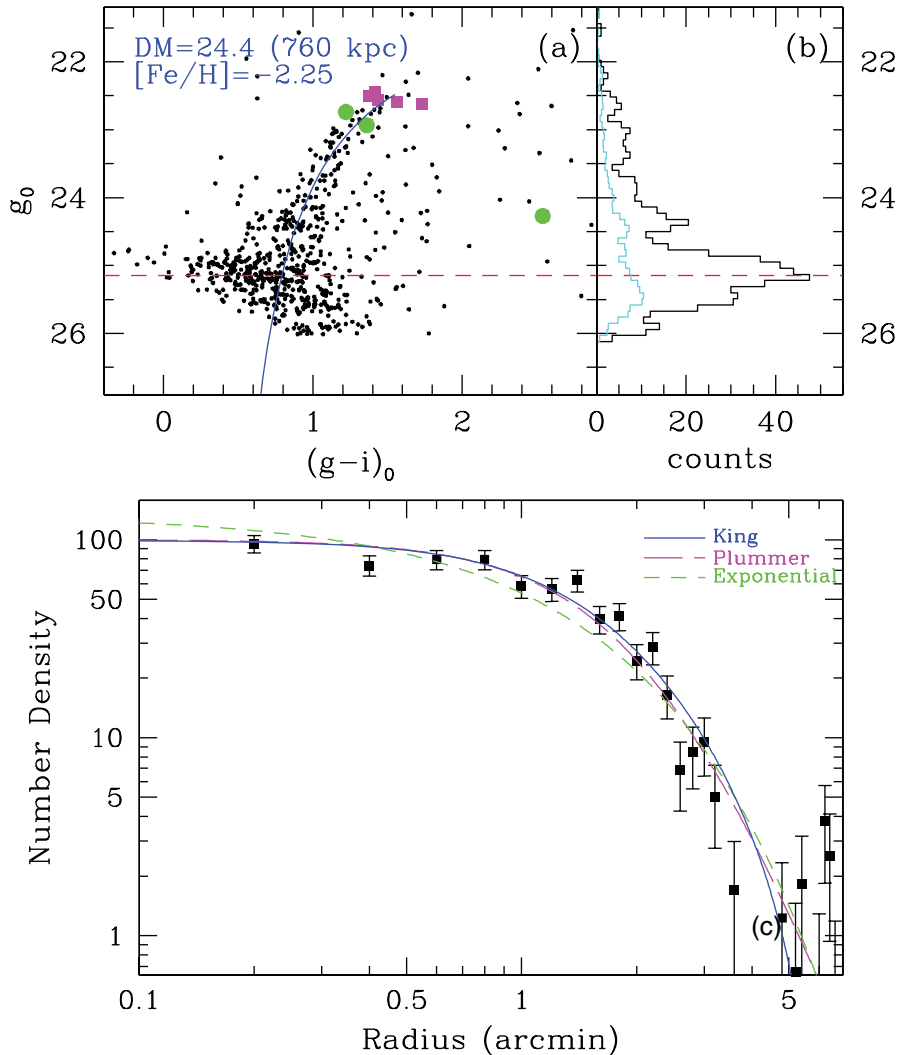

Figure 14. As Fig. 5, but for And IX. Isochrones are overlaid with [Fe/H] = −2.2 at the HB distance modulus of 24.5 (760 kpc). In plot (c), King (with $r_{\mathrm{t}} = 6.3$), Plummer and exponential profiles are overlaid, with respective half-light radii of 2.7 ± 0.2, 2.6 ± 0.1 and 2.5 ± 0.1 arcmin.

of 24.4 (760 kpc), also shown in Fig. 14, which is consistent with the findings of McConnachie et al. (2005a). For this reason we use their distance of $D = 765^{+5}_{-150}$ kpc for the remainder of our analysis. We calculate a total luminosity for the satellite at this distance of $L = 1.49^{+0.01}_{-0.07} \times 10^5 \, L_\odot$. These revised distance and luminosity values update the derived parameters of And IX with M_v becoming $-8.1^{+0.4}_{-0.1}$ (previously estimated as -8.3), and using the result from the Plummer profile, $r_{1/2} = 552^{+22}_{-110}$ pc, previously estimated as 530 pc (Chapman et al. 2005) and 300 pc (Harbeck et al. 2005).

As for the previous dSphs, we estimate the mean photometric metallicity of And IX by overlaying Dotter et al. (2008) isochrones (with age and abundance as detailed in Section 3.1) for the range of distances calculated above (615–770 kpc), giving a metallicity range for And IX of [Fe/H] $= -1.9$ to -2.3. We overlay the best-observed fit for the HB distance (765 kpc) in Fig. 14, with [Fe/H] $= -2.2$.

3.4.2 Spectroscopic properties

We display our kinematic results for And IX in Fig. 15. As with And XIII, the third line of the Ca II triplet in the stars observed in the And IX masks experiences significant contamination from OH skylines, so we derive velocities using the first two lines only. We identify nine stars as potential members of the satellite, at a velocity of ~ -200 km s^{-1} (highlighted by the heavy histogram) and an uncorrected $\sigma_v = 5.9$ km s^{-1}. Like And XIII, the systemic velocity of And IX places it much closer to the regime of Galactic foreground contamination. And IX also sits much closer (in projection) to M31 itself, so contamination from M31 halo stars is a larger problem than for the other satellites, due to the increased density in this region. Given both these factors, it is important for us to fully check our sample for any contaminants. One star (highlighted in pink) sits at a distance of roughly 10 arcmin from the centre of the satellite, which is beyond the tidal radius of And IX (6.6 arcmin). Further, when checking its position in the Subaru CMD and its spectroscopic metallicity when compared with the other eight candidates,

we find that this anomalous ninth star lies well off the RGB for the satellite [highlighted by the green circle that is located at $(g - i)_0 \sim 2.6$) in Fig. 14] and is far more metal rich spectroscopically when compared to the remaining eight stars ([Fe/H] $= -0.6$ versus [Fe/H] ~ -2 to -3 for the other candidates). For these reasons, we exclude this ninth star from the remainder of our analysis. Two other stars with velocities consistent with the systemic velocity of And IX at -220.9 and -209.8 km s^{-1} have very low TDR values of 2.7 and 1.6, respectively, falling well below our quality cut of TDR ≥ 3.5, indicating that the velocities for these objects are unreliable. We highlight these stars as green circles in Fig. 14 and we exclude these objects from the rest of our analysis, labelling them tentative members of And IX.

We display the spectra for each of the remaining eight stars in Fig. 15 also, with the top panel displaying the summed spectrum for the satellite. As was the case for And XIII, it can be seen that the Ca II$_{8662}$ is obscured by OH skylines for the majority of members. This is also evident in the composite spectrum, where the EW of the third line is measured to be significantly smaller than that of the first line (whereas in And XIII, the EW of the third line was enhanced). If we were to include this line in our analysis, it would cause us to underestimate the value of [Fe/H] for the dwarf. For this reason, we derive the metallicity for the satellite based on the Ca II$_{8498}$ and Ca II$_{8542}$ lines only, giving a metallicity for And IX of [Fe/H] $= -2.2 \pm 0.2$, which is a more metal-poor value than that found by Chapman et al. (2005) of [Fe/H] $= -1.5$, and more consistent with the value of [Fe/H] $= -2.0$ found by Harbeck et al. (2005) and the photometric metallicities we quote above. We shall discuss this discrepancy further in Section 4. Such a low metallicity would make this dwarf one of the most metal-poor M31 dSphs observed to date, comparable to And V (Davidge et al. 2002).

A maximum likelihood distribution for And IX is shown in Fig. 16 showing the best value when correcting from the instrumental measurements. From this technique we resolve $v_r = -207.7^{+2.7}_{-2.2}$ km s^{-1} and $\sigma_v = 4.5^{+3.6}_{-3.4}$ km s^{-1} (overlaid as a Gaussian curve in the top panel of Fig. 15). This dispersion is significantly lower than the
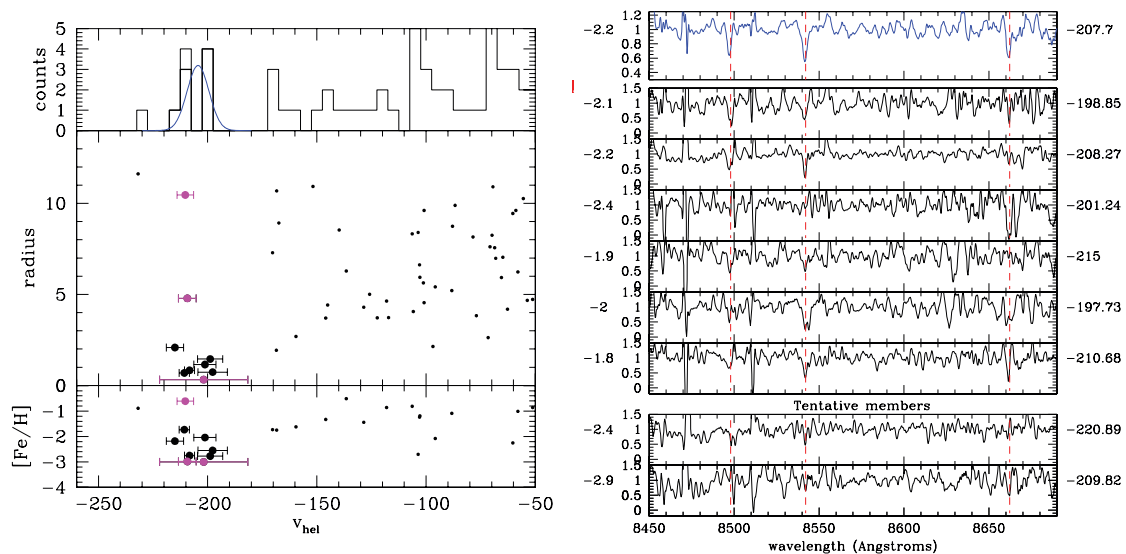

Figure 15. As Fig. 6, but for And IX. And IX can clearly be identified as a kinematic grouping at ~ -200 km s^{-1}. Of the nine stars at this velocity, eight are associated with And IX, with the ninth star lying well off the dwarf RGB (see Fig. 14, at a distance greater than 10 arcmin from the dwarf, and the two stars with low-quality cross-correlations (TDR < 3.5) highlighted in pink. The remaining eight stars are all found to be metal poor both photometrically (lower left-hand panel) and spectroscopically (right-hand panel), however, we note that two stars have unreliable velocity measurements. An analysis of the composite spectrum of the confirmed members yields [Fe/H] $= -2.2 \pm 0.2$.
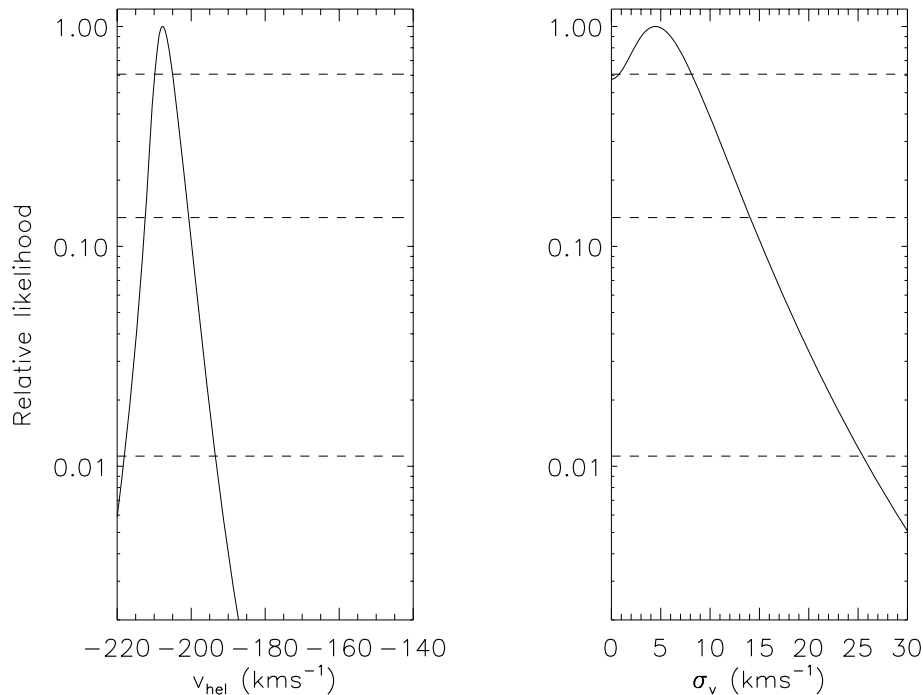
Figure 16. Likelihood distributions for And IX. Dashed lines represent the conventional 1σ, 2σ and 3σ confidence levels. The mean velocity for And IX is calculated to be $-207.7\,\mathrm{km\,s^{-1}}$, and the velocity dispersion is resolved by the technique as $4.5\,\mathrm{km\,s^{-1}}$.

value quoted in Chapman et al. (2005) of $\sigma_v = 6.8\,\mathrm{km\,s^{-1}}$, and this is likely due to the inclusion of non-members in their analysis as a result of the incorrect geometric model.

As for And XII, this measured velocity dispersion allows us to constrain the dark matter content of And IX (rather than just assign an upper limit, as for And XI and And XIII), assuming virial equilibrium. As before, we first use equation (2) to calculate the M/L of And IX. We derive $\mu_0 = 28.42\,\mathrm{mag\,arcsec^{-2}}$ and $S_0 = 0.155 \pm 0.01\,\mathrm{L_\odot\,pc^{-2}}$, and take $\sigma_0 = 4.5^{+3.6}_{-3.4}\,\mathrm{km\,s^{-1}}$ from our ML analysis, giving a most probable mass to light ratio $M/L = 78^{+100}_{-78}\,\mathrm{M_\odot/L_\odot}$. The implied mass is therefore $1.2^{+1.5}_{-1.2} \times 10^7\,\mathrm{M_\odot}$, potentially low mass when compared to other bright dwarfs ($M_V < -8$). Once again, applying equation (3) from Illingworth (1976), we calculate a mass of $9.9^{+12.6}_{-9.9} \times 10^6\,\mathrm{M_\odot}$ for And XI, with a corresponding $M/L = 66$, which again highlights the inconsistencies between the two methods.

Finally, applying equation (4) to our data, we estimate the mass contained within the half-light radius of And IX to be $M_{\mathrm{half}} = 6.5^{+8.3}_{-6.5} \times 10^6\,\mathrm{M_\odot}$. As these six And IX members sit within the half-light radius we determined in Section 3.4.1, we can consider our velocity dispersion to be a good approximation for the central dispersion of the dwarf.

4 DISCUSSION

4.1 Comparison with previous studies

The four dSphs analysed in this work have all been previously examined photometrically (Zucker et al. 2004; Harbeck et al. 2005; Martin et al. 2006) and, in the case of And IX and And XII, spectroscopically (Chapman et al. 2005, 2007). Here we discuss how our results compare with these other studies. For And XI, And XII and And XIII, the deeper photometric images from Subaru, combined with our spectroscopic results from DEIMOS, have enabled us to significantly improve upon previous values for structural parameters, such as half-light radius, distance etc., as derived in Martin et al. (2006) from CFHT-MegaCam data. We display our results for the structural properties of the dwarfs in Table 6 and their kinematic properties are displayed in Table 7. Whilst the absolute magnitudes mirror the initial values very closely, we find the other structural parameters for the satellites all differ significantly. In all three cases the half-light radii have approximately doubled from the values reported in Martin et al. (2006), and are now comparable to what is observed for MW dwarf galaxies of a similar luminosity, e.g. LeoT with $M_V = -7.1$ and $r_{1/2} = 170 \pm 15$ (Irwin et al. 2007; Simon &

Table 6. Structural properties of And XI, And XII, And XIII and And IX as derived in this work.

Property	And XI	And XII	And XIII	And IX
α	$0^{\mathrm{h}}\,46^{\mathrm{m}}\,21^{\mathrm{s}}$	$0^{\mathrm{h}}\,47^{\mathrm{m}}\,27^{\mathrm{s}}$	$0^{\mathrm{h}}\,51^{\mathrm{m}}\,51^{\mathrm{s}}$	$0^{\mathrm{h}}52^{\mathrm{m}}51\overset{\mathrm{s}}{.}1$
δ	$+33^\circ\,48'\,22''$	$+34^\circ\,22'\,29''$	$+33^\circ\,00'\,16''$	$+43^\circ\,11'\,48.6''$
$M_{V,0}$	$-6.9^{+0.5}_{-0.1}$	$-6.4^{+0.1}_{-0.5}$	$-6.7^{+0.4}_{-0.1}$	$-8.1^{+0.4}_{-0.1}$
$r_{1/2}$	145^{+24}_{-20} pc	289^{+70}_{-47} pc	203^{+27}_{-44} pc	552^{+22}_{-110} pc
Distance	760^{+10}_{-150} kpc	830^{+170}_{-30} kpc	910^{+30}_{-160} kpc	765^{+5}_{-150} kpc

Table 7. Kinematic properties of And XI, And XII, And XIII and And IX as derived in this work.

Property	And XI	And XII	And XIII	And IX
v_r (km s^{-1})	$-419.6^{+4.4}_{-3.8}$	$-558.4^{+3.2}_{-3.2}$	$-195.0^{+7.4}_{-8.4}$	$-207.7^{+2.7}_{-2.2}$
σ_v (km s^{-1})	4.6^a	$2.6^{+5.1}_{-2.6}$	$9.7^{+8.9}_{-4.5}$	$4.5^{+3.6}_{-3.4}$
[Fe/H]$_{spec}$	-2.0 ± 0.2	-2.1 ± 0.2	-1.9 ± 0.2	-2.2 ± 0.2
[Fe/H]$_{phot}$	-2.0	-1.9	-2.0	-2.2

^{a}Value quoted represents upper limit set by 1σ uncertainty from maximum likelihood analysis.

Table 8. Mass and M/L estimates for And XI, And XII, And XIII and And IX as derived in this work.

Property	And XI	And XII	And XIII	And IX
M/L_{RT86}(M$_\odot$/L$_\odot$)	152^a	55^{+152}_{-55}	821^{+1065}_{-538}	117^{+102}_{-100}
M_{RT86}(M$_\odot$)	$7.4 \times 10^{6\,a}$	$1.7^{+4.7}_{-1.7} \times 10^6$	$3.4^{+4.4}_{-2.2} \times 10^7$	$1.2^{+1.5}_{-1.2} \times 10^7$
M/L_{I76}	53^a	54^{+152}_{-54}	401^{+505}_{-252}	66^{+84}_{-66}
M_{I76}(M$_\odot$)	$2.6 \times 10^{6\,a}$	$1.6^{+4.6}_{-1.6} \times 10^6$	$1.6^{+2.1}_{-1.0} \times 10^7$	$6.5^{+8.3}_{-6.5} \times 10^6$
M_{half} (M$_\odot$)	$1.7 \times 10^{6\,a}$	$1.1^{+3.1}_{-1.1} \times 10^6$	$1.1^{+1.4}_{-0.7} \times 10^{7\,a}$	$6.5^{+8.3}_{-6.5} \times 10^6$

^{a}Value quoted represents upper limit set by 1σ uncertainty from maximum likelihood analysis.
RT86 refers to Richstone & Tremaine (1986), equation (1).
I76 refers to Illingworth (1976), equation (2).

Geha 2007). This is in contrast to the brighter M31 dSphs ($M_V < -8$), which are all observed to be larger than their MW counterparts of a similar luminosity (McConnachie et al. 2005b). We have also been able to derive distances to each of the dwarfs individually, whereas in Martin et al. (2006), photometry would only allow for an ensemble average. We find And XI to be the closest dwarf to us, lying at a distance of 760 kpc, with both And XII and And XIII being more distant, located at >800 kpc. In addition, we have re-analysed And XII spectroscopically, and our findings are largely consistent with those of Chapman et al. (2007).

For And IX, the structural properties we have derived from the Subaru data closely mirror the findings of Harbeck et al. (2005), Zucker et al. (2004) and Chapman et al. (2005). Our range of distances (615–770 kpc) and our HB distance estimate of 760 kpc agree well with the McConnachie et al. (2005a) result of 765 kpc (using a TRGB method). Our value for the half-light radius of 552^{+22}_{-110} pc is significantly larger than that quoted in Harbeck et al. (2005), but agrees with the findings of Chapman et al. (2006) and, like the remainder of its bright M31 brethren, it is more extended than its MW counterparts of a similar luminosity (e.g. Draco, with $M_V = -8.8$ and $r_{1/2} = 221$ pc; Martin et al. 2008). However, our re-reduction and analysis of the spectroscopic data with the correct geometrical model causes us to update a number of the parameters originally presented in Chapman et al. (2005). In our analysis, we resolve a velocity dispersion of only $4.5^{+3.6}_{-3.4}$ km s^{-1}, compared with their measured value of 6.8 km s^{-1}. Reassessing the combined spectrum for And IX, we find [Fe/H] $= -2.2 \pm 0.2$ for the satellite, significantly more metal poor than [Fe/H] $= -1.5$ reported by Chapman et al. (2005), largely due to excluding the Ca II$_{8662}$ line from our analysis, but also a result of the misclassification of member stars in Chapman et al. (2005). This new value is in much better agreement with the work of Harbeck et al. (2005) and Zucker et al. (2004) and is supported by our deep Subaru photometry.

4.2 Metallicities

The metallicity for each dwarf has been reassessed, with all four measured to be more metal poor than in previous works. There is

a good agreement between Subaru photometry (using Dartmouth isochrones) and spectroscopy for all the dSphs. In the past, much work has been undertaken to determine the metallicities of faint dSphs in the MW to see if they follow the same pattern of decreasing metallicity with decreasing luminosity as seen in their brighter counterparts (e.g. Mateo 1998). Until recently, this trend has appeared to break down in the fainter regime of dSphs, with low-luminosity satellites measured to be significantly more metal rich than expected. However, work undertaken by Kirby et al. (2008), measuring iron abundances with high and moderate resolution spectra from the HIRES and DEIMOS instruments on Keck, has shown that the faint satellites in the MW do contain sizable populations of very metal-poor stars. This result places them in line with the previously established trends, as shown in Fig. 17, where we plot the relation between absolute magnitude, M_v and [Fe/H] for dSphs. The green symbols represent the MW dwarfs and the dashed line shows the best fit to these satellites as determined by Kirby et al. (2008). We have also plotted the available information for the M31 dwarfs (blue inverted triangles) and it can be seen that they agree quite well with the relation at higher luminosities. For all four dwarfs analysed in this paper (plotted as red squares), it can be seen that they appear to be consistent with the relation within their 1σ error bars. This suggests that the relation between metallicity and absolute magnitude does not break down at these fainter luminosities.

Such a finding is perhaps unexpected, given work presenting evidence for a common mass scale for the haloes of the dSphs population. Strigari et al. (2008) conclude that the dSphs of the Local Group all have a common mass of $\sim 10^7$ M$_\odot$ within their central 300 pc. Work by Wolf et al. (2010) measuring the mass content of dSphs within their half-light radius, also presents evidence for a common mass scale for the haloes of the dSphs population, concluding that even the faintest MW dSphs are consistent with having formed within dark matter haloes of $\sim 3 \times 10^9$ M$_\odot$. Working within this framework of a common mass scale for the haloes of dSphs, one might expect to see metallicity level off at fainter luminosities, rather than continuing to decrease as, although the amount of luminous matter present in the system is decreasing, the amount of dark matter remains roughly constant. This would impose a limit to
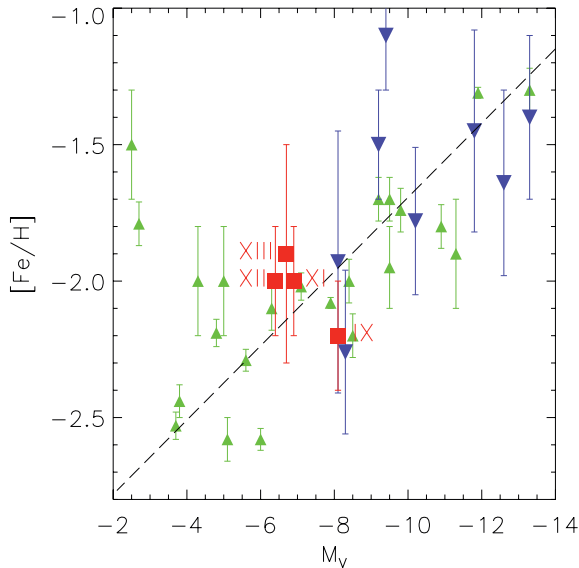
Figure 17. Mean values for [Fe/H] for both M31 and MW satellites versus absolute magnitude (M_V). A line of best fit to the MW dwarfs, taken from Kirby et al. (2008) is overplotted. Values for the M31 dwarfs were taken from Da Costa, Armandroff & Caldwell (2002), Da Costa et al. (2000), Davidge et al. (2002), Grebel & Guhathakurta (1999), McConnachie et al. (2005a), McConnachie & Irwin (2006b), McConnachie et al. (2008), Irwin et al. (2008), Kalirai et al. (2009) and Kalirai et al. (2010), and for the MW, Koch & Grebel (2006), Koch et al. (2007a,b), Martin et al. (2007), Ibata et al. (2006), Kirby et al. (2008), and Mateo (1998). MW objects are plotted as green triangle, M31 objects as blue inverted triangles and our results are plotted as red squares.

the amount of metals that could escape the gravitational potential of the galaxy, preventing dSphs from becoming overly metal poor. However, a similar study by Walker et al. (2009b) (also measuring the mass content of dSphs within the half-light radius) finds that, whilst the dSphs of the MW are broadly consistent with having formed within a universal dark matter halo, there is significant scatter in this relationship at the faint end of the luminosity spectrum which could indicate that these fainter dwarf galaxies are residing in less massive haloes. This would allow them to expel more of their metals at early epochs, resulting in lower metallicities, which could explain this continuation of the trend seen in brighter dwarfs. Another explanation is provided by Salvadori & Ferrara (2009) who model the merger history of the MW from $z = 20$ to the present day to investigate the nature of 'ultrafaint' dSphs (such as those discussed in this work); they find that the low metallicities of these objects are the result of lower gas metallicity at the time of their formation, and suppression of star formation during their evolution.

4.3 The dynamics of M31's dSph population

Recent work by Walker et al. (2009b) and Wolf et al. (2010), investigating the common mass scale for dSphs, demonstrates a clear correlation between the velocity dispersion and half-light radius for MW dSphs. In Fig. 18 we plot σ_v versus $r_{1/2}$ for all MW dwarfs with published velocity dispersions (taken from Walker et al. 2009b), the available M31 data points (Peñarrubia et al. 2008a; Letarte et al. 2009, And XVI is shown as an upper limit) and overplot the best-fitting power law, Navarro–Frenk–White (NFW) and cored profiles from Walker et al. (2009b) to these data. The upper limit determined for And XI is displayed as an open red square, and the resolved measurements for And XII, And XIII and And IX are shown as filled squares. Interestingly, And XII and And IX both fall below these relations within their 1σ uncertainties. Whilst these results could be an artefact of small sample size and low S/N, given the scarcity of available kinematic data for the dSph population of M31, it is useful to consider the implications of such findings. If the dispersions of these dwarfs do fall significantly below established trends, could this be an indication that the dSph companions of M31 are dynamically colder than their MW counterparts? The brighter dwarf galaxies of M31 are already observed to differ from those orbiting the MW, with work by McConnachie et al. (2005b) showing that M31 dSphs with $M_V < -8$ are spatially more extended than MW dSphs of the same luminosity (though it is unclear what the origin of this difference is). Curiously, if M31 and MW dSphs inhabit systematically similar haloes (i.e. the mass and extent of the stellar population is independent of the mass and extent of the dark matter halo), one would expect to see the opposite trend, with the velocity dispersions of M31 satellites being roughly double those of MW dwarfs of the same luminosity (Peñarrubia et al. 2008a). It is also worth mentioning that a recent study of And I, And II, And III, And VII, And X and And XIV (Kalirai et al. 2009, 2010) finds that a number of these objects also appear to be dynamically colder than their MW counterparts.

These colder dispersions translate to lower masses for And IX and And XII (see Table 8), as the three mass estimators we have used within this work are all proportional to the square of the dispersion (as shown in equations 2–4). Comparison of the masses of Local Group dSphs has previously proven to be problematic. A variety of mass estimators (as discussed in Section 3.1.2) used throughout the literature, and the differing radial extent of the dSphs probed by kinematic surveys make it difficult to ensure that, when making comparisons between dSphs within the Local Group, we are truly comparing like with like. Historically, the masses of dSphs have been discussed in terms of the Mateo (1998) relation between M/L and the luminosity of dwarf galaxies, which was established in relation to Local Group dSphs with $M_V < -8$. This relation is displayed in the top right-hand panel of Fig. 18, with M/L values for satellites from both the MW and M31 taken from the literature plotted also. We display the upper limits on M/L (using the Richstone & Tremaine 1986 mass estimator) for And XI (open red square), and plot the calculated values for And IX, And XII and And XIII (filled red squares), where the error bars represent their 1σ uncertainties. We note that the lower limits for three of the four dwarfs (And XI, And XII and And IX) are consistent with zero. And IX, And XI and And XIII are consistent with this relation within their 1σ error bars, but And XII joins the ultrafaint MW dwarfs as an outlier.

The work by Walker et al. (2009b) and Wolf et al. (2010) has shown that the mass within the half-light radius of dispersion supported galaxies, such as dSphs, can be accurately estimated with only mild assumptions about the spatial variation of the stellar velocity dispersion anisotropy, unlike the two methods discussed above. Furthermore, by considering only the mass contained within $r_{1/2}$, one can negate the effect of the differing radial extents probed by surveys, making comparisons between the masses of the dSphs more meaningful. Their conclusion that there is a tight correlation between velocity dispersion (and hence, mass) and half-light radius for MW dSphs is consistent with the idea that all the MW dSphs (including those with $M_V > -8$) are formed with a 'universal' halo profile (as discussed in Section 4.2). In the bottom left-hand panel of Fig. 18, we plot M_{half} versus $r_{1/2}$ for And IX, And XI, And XII and And XIII along with the other Local Group dSphs for which
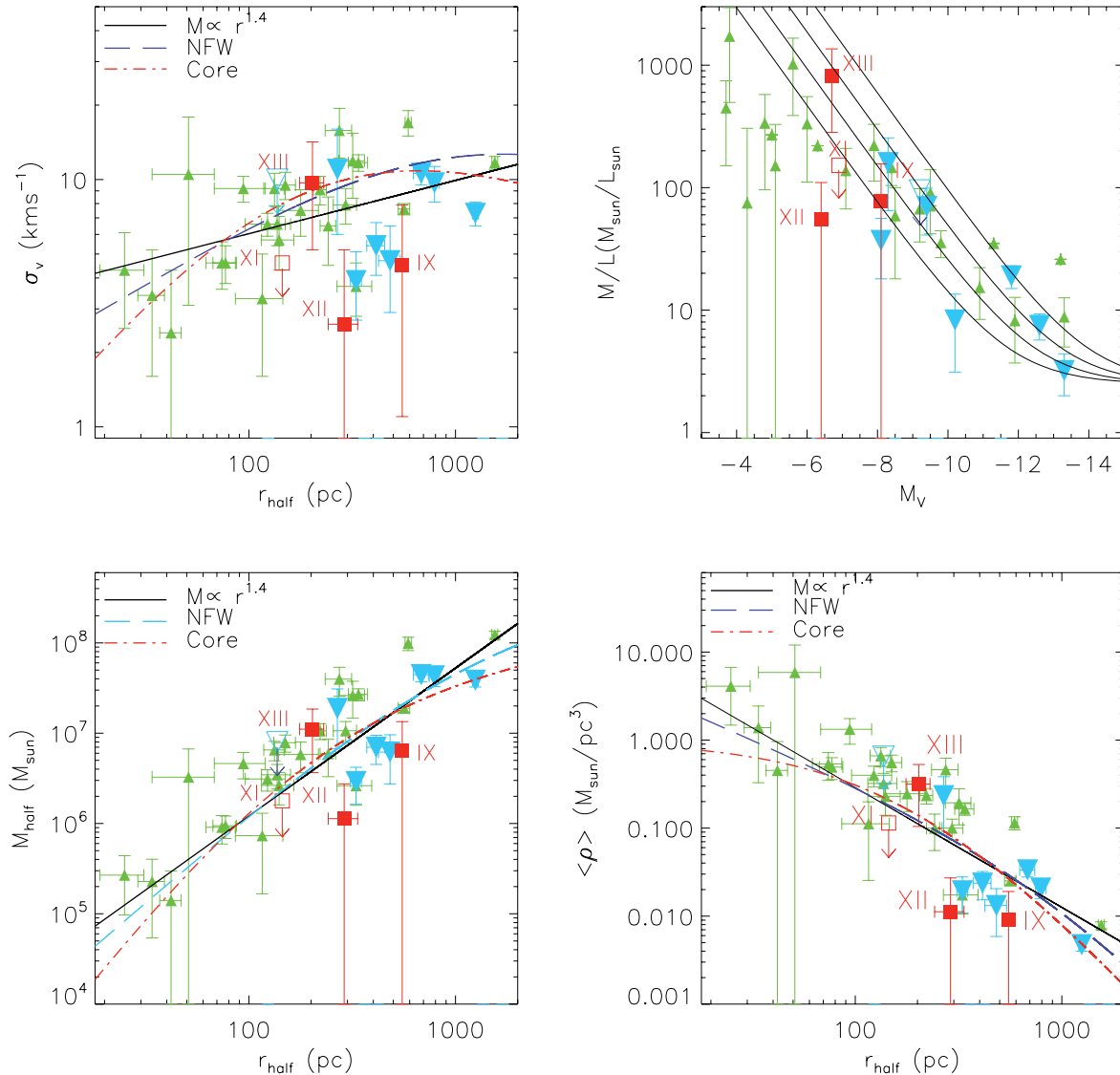
Figure 18. For all figures, the symbols used are as for Fig. 17. In all cases, filled symbols represent resolved measurements, and open symbols represent upper limits set by 1σ uncertainties. References for MW and M31 data are as specified in Fig. 17, plus Walker et al. (2009b) and references therein. Top left: global velocity dispersion for MW and M31 dSphs are plotted as a function of their half-light radius, The best-fitting mass profiles (based on power law, NFW and cored halo profiles) for the MW dSph population, from Walker et al. (2009b) (transferred into the $\sigma_v - r_{1/2}$ plane) are overplotted. Top right: comparison of the M/L and luminosity estimates (M_v) for the faintest known dwarf galaxies from both the MW and M31 with central velocity dispersion estimates. The Mateo (1998) relations for dSphs are overplotted as black lines, representing curves of constant dark matter halo mass (1, 2, 4, $8 \times 10^7 \, \mathrm{M_\odot}$ from bottom to top), assuming a stellar M/L of $2.5 \, \mathrm{M_\odot/L_\odot}$. And XII appears to be an outlier to this relation. Bottom left: comparison of the mass contained within the half-light radius (M_{half}) as a function of $r_{1/2}$, with the Walker et al. (2009b) mass profiles overplotted. Both And IX and And XII fall below these relations. Bottom right: mean density ($\langle \rho \rangle$) within the half-light radius is plotted, with the same mass profiles as in the top right-hand panel. Again, And IX and And XII appear to be outliers to these relations.

kinematic data are available, and overplot the best-fitting power law, NFW and cored profiles from Walker et al. (2009b) to these data. In this instance, we can see that And IX and And XII fall below these relations within their 1σ errors, whereas And XIII conforms to the MW trends.

In terms of its mass and dispersion, And IX in particular seems to stand out. At $M_V = -8.1$ it is similar in terms of its absolute brightness to the MW dwarfs, Draco and Ursa Minor ($M_V = -8.8$ and -8.4, respectively; Martin et al. 2008), and has a half-light radius that is roughly twice that of these dwarfs (552 versus $\sim$200 pc), however, we measure a dispersion of only $4.5 \, \mathrm{km \, s^{-1}}$ for And IX, compared with 9.1 and $9.6 \, \mathrm{km \, s^{-1}}$ for Draco and Ursa Minor (Walker

et al. 2007, 2009b). This suggests that And IX inhabits a dark matter halo that is significantly different to those of the brighter MW dSphs.

In the case of And XII, whilst it does fall below the profiles of Walker et al. (2009b), it is quite similar in terms of both structure and kinematics to several of its MW counterparts at a similar luminosity, e.g. Hercules and Leo IV (with $M_V = -6.0$ and -5.1, $r_{1/2} = 330$ and 116 pc, $\sigma_v = 3.7$ and $3.3 \, \mathrm{km \, s^{-1}}$, respectively; Walker et al. 2009b). Perhaps then, it is only these 'ultrafaint' dSphs ($M_V > -8$) that reside in significantly different dark matter haloes, with And IX being a curious exception. It is worth noting that the upper limit of $\sigma_v = 4.7 \, \mathrm{km \, s^{-1}}$ that we attach to And XI ($M_V = -6.9$,

$r_{1/2} = 145$ pc) suggests that this faint dwarf is also an outlier to these relations.

If these satellites truly fall below these relations, the question becomes, are they embedded in a less massive dark matter haloes than their MW counterparts, constituting a population of lower mass dwarfs whose detection has thus far eluded us? These lower values of M/L and M_{half} are unlikely to be the result of tidal mass stripping, as the process tends to increase rather than decrease values of M/L (Peñarrubia, Navarro & McConnachie 2008b). This is because the tightly bound central dark matter 'cusp' of a dwarf is more resilient to tidal disruption than the stellar component of the galaxy, causing the object to become more dark matter dominated as it undergoes tidal stripping. It should be noted that the mass estimators of Richstone & Tremaine (1986) and Illingworth (1976) are measures of the *central* population of the galaxies, where the stars can be used as tracers, therefore, they are only true throughout the dwarf if the M/L is constant throughout the system. It could be that these dwarfs reside in more massive dark matter haloes, such as is seen for brighter galaxies, and these central low-mass estimates could imply lower central densities for the two dwarfs, making them peculiar objects. To examine this possibility further, we plot the mean total (i.e. baryonic plus dark) mass density of the dSphs within the half-light radius in the bottom right-hand panel of Fig. 18, and it can be seen that both And IX and And XII have a lower density than would be expected for their size.

5 CONCLUSION

We have studied the four faint M31 satellites, And IX, And XI, And XII and And XIII, using spectroscopic data from Keck II/DEIMOS and Subaru/Suprime-Cam. Using our spectroscopic results, we have identified probable members for each galaxy and constrained their systemic velocities. Owing to our low S/N and small sample sizes, we are unable to resolve a velocity dispersion for And XI. Instead we use the 1σ confidence level from the maximum likelihood technique as an upper limit for the satellite. In the case of And IX, And XII and And XIII we resolve $\sigma_v = 4.5^{+3.6}_{-3.4}$, $\sigma_v = 3.8^{+3.9}_{-3.8}$ and $\sigma_v = 9.7^{+8.9}_{-4.5}$ km s^{-1} for each dwarf, respectively, though we note that And XII is consistent with 0 km s^{-1} within its 1σ errors and the measurement of And XIII's dispersion is based on only three stars. Measuring the average spectroscopic metallicity of each satellite from their composite spectra, we find that all four satellites are metal poor ([Fe/H] ~ -2.0). Such metallicities are comparable to what is observed in MW dSphs of a similar luminosity, suggesting that the established relation between M_V and [Fe/H] observed in both the brighter classical MW dwarfs (Mateo 1998) and the fainter MW dSphs (Kirby et al. 2008) continues down to luminosities of $M_V > -6.4$ in the M31 dSphs population.

Finally, we place the velocity dispersions and masses for these dSphs in the context of the universal dark matter halo profiles established for the MW dwarf galaxies in Walker et al. (2009b) and find that both And IX and And XII have lower dispersions than would be expected for dSphs of their size, similar to a number of dSphs studied by Kalirai et al. (2010). If these results are verified, it could imply that the dSph population of M31 is dynamically colder than that of the MW, which is unexpected, given their larger spatial extent. Such results also imply that the mass contained within the half-light radii of these dwarfs is also lower than what is typically observed in their MW counterparts of a similar size, and suggests that these dSphs may reside in lower density dark matter haloes.

The results we have presented here indicate that, in terms of their dynamical properties, these satellites at the faint end of the dSph spectrum do not behave as expected from previous studies. Further spectroscopic observations of faint objects similar to these (e.g. those found by McConnachie et al. 2008) will undoubtedly help us to better understand this low-luminosity regime, and shed light on to the behaviour of these faintest of galaxies.

REFERENCES

Allende Prieto C., 2007, AJ, 134, 1843
Bellazzini M., Gennari N., Ferraro F. R., Sollima A., 2004, MNRAS, 354, 708
Belokurov V. et al., 2007, ApJ, 654, 897
Belokurov V. et al., 2008, ApJ, 686, L83
Chapman S. C., Ibata R., Lewis G. F., Ferguson A. M. N., Irwin M., McConnachie A., Tanvir N., 2005, ApJ, 632, L87
Chapman S. C., Ibata R., Lewis G. F., Ferguson A. M. N., Irwin M., McConnachie A., Tanvir N., 2006, ApJ, 653, 255
Chapman S. C. et al., 2007, ApJ, 662, L79
Chen Y. Q., Zhao G., Zhao J. K., 2009, ApJ, 702, 1336
Côté P., Mateo M., Olszewski E. W., Cook K. H., 1999, ApJ, 526, 147
Da Costa G. S., Armandroff T. E., Caldwell N., Seitzer P., 2000, AJ, 119, 705
Da Costa G. S., Armandroff T. E., Caldwell N., 2002, AJ, 124, 332
Davidge T. J., Da Costa G. S., Jørgensen I., Allington-Smith J. R., 2002, AJ, 124, 886
Dotter A., Chaboyer B., Jevremovic D., Kostov V., Baron E., Ferguson J. W., 2008, ApJS, 178, 89
Faber S. M. et al., 2003, in Iye M., Moorwood A. F. M., eds, Proc. SPIE Conf. Ser. Vol. 4841, The DEIMOS Spectrograph for the Keck II Telescope: Integration and Testing. SPIE, Bellingham, p. 1657
Ferraro F. R., Paltrinieri B., Rood R. T., Fusi Pecci F., Buonanno R., 2000, ApJ, 537, 312
Geha M., Willman B., Simon J. D., Strigari L. E., Kirby E. N., Law D. R., Strader J., 2009, ApJ, 692, 1464
Girardi L., Grebel E. K., Odenkirchen M., Chiosi C., 2004, A&A, 422, 205
Girardi L. et al., 2008, PASP, 120, 583
Grebel E. K., Guhathakurta P., 1999, ApJ, 511, L101
Harbeck D., Gallagher J. S., Grebel E. K., Koch A., Zucker D. B., 2005, ApJ, 623, 159
Ibata R., Chapman S., Ferguson A. M. N., Lewis G., Irwin M., Tanvir N., 2005, ApJ, 634, 287
Ibata R., Chapman S., Irwin M., Lewis G., Martin N., 2006, MNRAS, 373, L70
Ibata R., Martin N. F., Irwin M., Chapman S., Ferguson A. M. N., Lewis G. F., McConnachie A. W., 2007, ApJ, 671, 1591
Illingworth G., 1976, ApJ, 204, 73
Irwin M., Lewis J., 2001, New Astron. Rev., 45, 105
Irwin M. J. et al., 2007, ApJ, 656, L13
Irwin M. J., Ferguson A. M. N., Huxor A. P., Tanvir N. R., Ibata R. A., Lewis G. F., 2008, ApJ, 676, L17
Kalirai J. S. et al., 2006, ApJ, 648, 389
Kalirai J. S. et al., 2009, ApJ, 705, 1043
Kalirai J. S. et al., 2010, ApJ, 711, 671
Kirby E. N., Simon J. D., Geha M., Guhathakurta P., Frebel A., 2008, ApJ, 685, L43
Klypin A., Kravtsov A. V., Valenzuela O., Prada F., 1999, ApJ, 522, 82
Koch A., Grebel E. K., 2006, AJ, 131, 1405
Koch A., Grebel E. K., Klenya J. T., Wilkinson M. I., Harbeck D. R., Gilmore G. F., Wyse R., Evans W., 2007a, AJ, 133, 270
Koch A., Wilkinson M. I., Klenya J. T., Gilmore G. F., Grebel E. K., Hackey A. D., Evans N. W., Wyse R. F., 2007b, ApJ, 657, 241
Koposov S. et al., 2008, ApJ, 686, 279

Letarte B. et al., 2009, MNRAS, 400, 1472

McConnachie A. W., Irwin M. J., 2006a, MNRAS, 365, 902

McConnachie A. W., Irwin M. J., 2006b, MNRAS, 365, 1263

McConnachie A. W., Irwin M. J., Ferguson A. M. N., Ibata R. A., Lewis G. F., Tanvir N., 2004, MNRAS, 350, 243

McConnachie A. W., Irwin M. J., Ferguson A. M. N., Ibata R. A., Lewis G. F., Tanvir N., 2005a, MNRAS, 356, 979

McConnachie A., Irwin M., Chapman S., Ibata R., Ferguson A., Lewis G., Tanvir N., 2005b, in Jerjen H., Binggeli B., eds, IAU Colloq. 198, Near-Fields Cosmology with Dwarf Elliptical Galaxies. Cambridge Univ. Press, Cambridge, p. 84

McConnachie A. et al., 2008, ApJ, 688, 1009

McConnachie A. W. et al., 2009, Nat, 461, 66

Mackey A. D. et al., 2010, MNRAS, 401, 533

Majewski S. R. et al., 2007, ApJ, 670, L9

Marcolini A., D'Ercole A., Battaglia G., Gibson B. K., 2008, MNRAS, 386, 2173

Martin N. F., Ibata R. A., Irwin M. J., Chapman S., Lewis G. F., Ferguson A. M. N., Tanvir N., McConnachie A. W., 2006, MNRAS, 371, 1983

Martin N. F., Ibata R. A., Chapman S. C., Irwin M., Lewis G. F., 2007, MNRAS, 380, 281

Martin N. F., de Jong J. T. A., Rix H.-W., 2008, ApJ, 684, 1075

Martin N. F. et al., 2009, ApJ, 705, 758

Mateo M. L., 1998, ARA&A, 36, 435

Moore B., Ghigna S., Governato F., Lake G., Quinn T., Stadel J., Tozzi P., 1999, ApJ, 524, L19

Muñoz R. R., Majewski S. R., Johnston K. V., 2008, ApJ, 679, 346

Niederste-Ostholt M., Belokurov V., Evans N. W., Gilmore G., Wyse R. F. G., Norris J. E., 2009, MNRAS, 398, 1771

Oh K. S., Lin D. N. C., Aarseth S. J., 1995, ApJ, 442, 142

Peñarrubia J., McConnachie A. W., Navarro J. F., 2008a, ApJ, 672, 904

Peñarrubia J., Navarro J. F., McConnachie A. W., 2008b, ApJ, 673, 226

Piatek S., Pryor C., 1995, AJ, 109, 1071

Richstone D. O., Tremaine S., 1986, AJ, 92, 72

Robin A. C., Reylé C., Derrière S., Picaud S., 2004, A&A, 416, 157

Salvadori S., Ferrara A., 2009, MNRAS, 395, L6

Schlegel D. J., Finkbeiner D. P., Davis M., 1998, ApJ, 500, 525

Simon J. D., Geha M., 2007, ApJ, 670, 313

Sohn S. T. et al., 2007, ApJ, 663, 960

Somerville R. S., 2002, ApJ, 572, L23

Strigari L. E., Bullock J. S., Kaplinghat M., Simon J. D., Geha M., Willman B., Walker M. G., 2008, Nat, 454, 1096

Tollerud E. J., Bullock J. S., Strigari L. E., Willman B., 2008, ApJ, 688, 277

Walker M. G., Mateo M., Olszewski E. W., Gnedin O. Y., Wang X., Sen B., Woodroofe M., 2007, ApJ, 667, L53

Walker M. G., Belokurov V., Evans N. W., Irwin M. J., Mateo M., Olszewski E. W., Gilmore G., 2009a, ApJ, 694, L144

Walker M. G., Mateo M., Olszewski E. W., Peñarrubia J., Wyn Evans N., Gilmore G., 2009b, ArXiv e-prints

Wilkinson M., Klenya J., Evans W., Gilmore G., Irwin M., Grebel K., 2004, ApJ, 611, L21

Willman B., Governato F., Dalcanton J. J., Reed D., Quinn T., 2004, MNRAS, 353, 639

Willman B. et al., 2005a, AJ, 129, 2692

Willman B. et al., 2005b, ApJ, 626, L85

Wolf J., Martinez G. D., Bullock J. S., Kaplinghat M., Geha M., Munoz R. R., Simon J. D., Avedo F. F., 2010, MNRAS, doi:10.1111/j.1365-2966.2010.16753.x

Zucker D. B. et al., 2004, ApJ, 612, L121

Zucker D. B. et al., 2006a, ApJ, 643, L103

Zucker D. B. et al., 2006b, ApJ, 650, L41

Zucker D. B. et al., 2007, ApJ, 659, L21

This paper has been typeset from a T_EX/L^AT_EX file prepared by the author.